Neuronal Circuits of NREM Sleep Control in the Basal Forebrain and Midbrain

By

Wei-Cheng Chang

A dissertation submitted in partial satisfaction of the

requirements for the degree of

Doctor of Philosophy

in

Molecular and Cell Biology

in the

Graduate Division

of the

University of California, Berkeley

Committee in charge:

Professor Yang Dan, Chair

Professor John Ngai

Professor Michael DeWeese

Professor Stephan Lammel

Spring 2018

Abstract

Neuronal Circuits of NREM Sleep Control in the Basal Forebrain and Midbrain

By

Wei-Cheng Chang

Doctor of Philosophy in Molecular and Cell Biology

University of California, Berkeley

Professor Yang Dan, Chair

Sleep is a fundamental behavior in the animal kingdom. It is essential for optimal cognition, general health, immune function and neuronal plasticity. Irregular or insufficient sleep may cause emotional disturbances, abnormal homeostasis of physiological functions. About 30% adults in the US suffered from insomnia. Therefore, understanding of the sleep-wake circuit will contribute to the cure of not only sleep disorders, but also other psychiatric diseases. A crucial step in understanding the neural circuits controlling sleep is to identify the sleep neurons. In my thesis, I used transgenic Cre mouse lines, virus-mediated circuit tracing, and optogenetic manipulation to identify the sleep-promoting neurons and dissect the neural circuits for controlling sleep and arousal.

In chapter 2: The basal forebrain (BF) contains a spatially intermingled diverse population of neurons that play key roles in multiple brain functions, including sleep-wake regulation, attention, and learning/memory. For sleep-wake regulation, the cholinergic, glutamatergic, and parvalbumin-expressing (PV) GABAergic neurons have been shown to promote wakefulness, whereas the somatostatin-expressing (SOM) GABAergic neurons promote NREM sleep. To understand how these cell types in the same area have different functions in sleep-wake regulation, we used rabies virus -mediated monosynaptic retrograde tracing to label the inputs and adeno-associated virus to trace axonal projections. We identified numerous brain areas connected to the BF. These results reveal the long-range wiring diagram of the BF circuit with highly convergent inputs and divergent outputs and point to both functional commonality and specialization of different BF cell types.

In chapter3: We identified the neurotensin (NTS) neurons in the preoptic area, posterior thalamus (pTh), and ventrolateral periaqueductal gray (vlPAG) as NREM sleep-promoting neurons based on optogenetic manipulation. Using rabies virus-mediated monosynaptic retrograde tracing combined with fluorescent in situ hybridization (FISH) experiment, we also showed that cholecystokinin (CCK) and calcitonin gene-related peptide alpha (Calca) neurons in the EW (CCK^{EW}), and NTS neurons in the vlPAG (NTS^{vlPAG}) form reciprocal connections to each other. These cell types may cooperate to promote NREM sleep.

Acknowledgements

The work of Chapter 2, “Cell type-specific long range connections of basal forebrain circuit”, was published in eLife in 2016. It is my pleasure to collaborate with the following individuals:

Authors: Johnny Phong Do+, Min Xu+, Seung-Hee Lee+, Wei-Cheng Chang, Siyu Zhang, Shinjae Chung, Tyler J. Yung, Jiang Lan Fan, Kazunari Miyamichi, Liqun Luo, and Yang Dan (+ These authors contributed equally to this work)

Author Contributions: J.D., and M.X. organized the data and wrote the software for data analyses, S.-H. L., and Y.D conceived and designed the experiments, W.-C. C., S.Z., S.C., T.J. Y., and J.L.F. performed the experiments, W.-C. C. also responsible for virus preparation, K.M. and L.L. provided crucial reagents and vectors for RV production. J.D., M.X., S.-H. L., W.-C. C., S.Z., S.C., and Y.D. wrote the manuscript.

The work of Chapter 3, “Neurotensin Neuronal Circuits for NREM sleep control”, was help by many people in my lab. It is hard for myself to finish this project without other people’s help. I am grateful to Shuming An, Chenyan Ma, Peng Zhong and Zhe Zhang for their support and animal behavior experiment.

Table of Contents

CHAPTER 1
The regulation of Sleep

Introduction

Sleep is a naturally occurring, reversible, and periodic behavior. It is an essential biological process that has been observed in most species in the animal kingdom. Human beings spend nearly one-third of time in sleep state (Savage and West, 2007). It is worthwhile for people to conduct research to understand why sleep is important to our life and what kind of mechanism will induce sleep behavior. Here, I summarize some previous literature to help us understand the mechanism and function of sleep.

Measurements of sleep

People usually define sleep as immobility and eye-closing. However, it is not good enough to distinguish between contemplation, rest, and sleep. The first major advance in sleep research was the development of technology, which allowed researchers to record brain activity. In 1924, Dr. Hans Berger (1873-1941) recorded the first human EEG (Haas, 2003). He found that EEG signal would dramatically change during wakefulness, while the signal is in slow frequency during sleep. In mammals, sleep can be divided into 2 stages called non-rapid eye movement (NREM) and rapid eye movement (REM) sleep (Hobson, 2005). The muscle electrical activity was also recorded by a electromyogram (EMG). The EEG and EMG signals provide the scientific data to distinguish wakefulness and sleep. Wakefulness is characterized by low amplitude and high frequency in the EEG and high muscle activity in the EMG. NREM is characterized by high amplitude and low frequency (0.5-4 Hz, delta oscillation) in the EEG and lower muscle activity in the EMG. During REM sleep, the EEG signal is similar to that of wakefulness and corresponds with near-total-loss muscle activity called muscle atonia. Interestingly, the EEG signal shows theta oscillation (8 Hz) during REM sleep in rodent. Ultimately, it is now more precise to distinguish between wakefulness, NREM sleep, and REM sleep through the EEG and EMG signal.

Neural circuits for wakefulness

In the early nineteenth century, a type of viral infected encephalitis swept through Europe and North America. The apparent symptoms of the encephalitis were excessive sleep but unaffected normal cognitive function. After investigation, Dr. Von Economo found a lesion at the junction between the diencephalon and the midbrain in patients' brains in 1930. This provided the first hint that some neurons in the area would affect wakefulness. A few years later, Dr. Moruzzi and Magoun showed that excessive sleep was caused by an ascending arousal pathway that begins in the rostral pons to the midbrain reticular formation (Moruzzi and Magoun, 1949).

Currently, the ascending arousal pathway is divided into two major branches. The first branch sends projections to the thalamus and cortex, which originates from the cholinergic cell groups of the pedunculopontine tegmentum (PPT) and laterodorsal tegmental nucleus (LDT) in the upper pons (Hallanger et al., 1987). This is a crucial pathway for transmitting arousal information from the upper brain stem to the cortex. These neurons have higher firing rates during wakeful and REM states compared to the NREM state (Strecker et al., 2000). The second branch transmits the arousal signal by providing monoaminergic neurons innervation of the

hypothalamus, basal forebrain (BF) and cerebral cortex (Saper, 1985). This pathway comprises the noradrenergic locus coeruleus (LC), serotoninergic raphe nuclei, dopaminergic ventral periaqueductal gray matter, and histaminergic tuberomammillary nucleus (TMN) (Saper et al., 2001).

The orexin neurons in the lateral hypothalamus are thought to sustain and promote wakefulness. The cholinergic neurons of the BF are excited by orexin neurons, resulting in cortical activation and wakefulness (Eggermann et al., 2001). In addition, orexin neurons also reinforce the arousal pathway by augmenting the signals from the LC and TMN to the cortex through BF (Peyron et al., 1998). Ablation of orexin neurons in mice resulted in phenotypic narcolepsy (Hara et al., 2001). All of the monoaminergic neurons fire at higher rates during wakefulness and slow down in REM and NREM sleep, except that cholinergic neurons of the BF are active during both wake and REM sleep (Lee et al., 2005).

Neural circuits for NREM Sleep

The preoptic area (POA) plays an important role in the regulation of NREM sleep based on the lesion study in the rat (Nauta, 1946) and muscimol injection experiments in the cat (Sallanon et al., 1989). The extracellular recording also showed that there are sleep-active neurons in the POA and BF (Szymusiak and McGinty, 1986). C-Fos protein detection following sustained sleep revealed a GABAergic neuron population located in the ventrolateral preoptic area (VLPO) that innervates the histaminergic TMN (Sherin et al., 1996). GABAergic VLPO neurons also send projections to a wide range of the ascending arousal nucleus such as LC, raphe nuclei and orexin neurons (Sherin et al., 1998). Thus, the inhibition of the wake-promoting areas may be a mechanism to promote sleep.

Though most neurons in the BF are wake-active neurons, there are still some NREM-active neurons in the BF. Most of the NREM-active neurons in the BF are GABAergic (Hassani et al., 2009). Lesion of the BF in cats causes decreesed sleep (McGinty and Sterman, 1968)., while selective activation of somatostatin GABAergic neurons by optogenetics in the BF promotes NREM sleep. BF somatostatin neurons may induce NREM sleep by inhibiting local wake-active BF neurons (Xu et al., 2015).

Circadian Regulation of Sleep

The suprachiasmatic nucleus (SCN) is situated bilaterally in the hypothalamus, just above the optic chiasm. The SCN is considered as a master circadian clock which is influenced by light-dark cycle to set a 24 hour rhythm (Daan et al., 1984). The pacemaker role of the suprachiasmatic nucleus in a mammalian circadian system was tested by neural transplantation by using a mutant strain of hamster that exhibits a short circadian period. The transplantation of SCN from normal hamsters to mutant strain hamsters restores normal periodicity; mutant to normal transplantation has the opposite effect (Ralph et al., 1990). The restored rhythms always exhibited the periodicity of the donor genotype. The results imply the overt circadian rhythm is determined by cells of the suprachiasmatic region.

The SCN provides a massive projection to the dorsomedial hypothalamus (DMH) and subparaventricular zone (SPZ) (Lu et al., 2001). Excitotoxic lesions of the DMH reduce circadian rhythms of wakefulness by 80%. It has been shown that DMH sends a mainly GABAergic projection to the VLPO and glutamatergic projection to the orexin neurons in the lateral hypothalamus (Chou et al., 2003). Excitotoxic lesions of the ventral SPZ reduces the circadian index of sleep by 90% but had little effect on body temperature (Lu et al., 2001). Researcher purposed that SPZ neurons innervate VLPO predominantly expressed glutamatergic markers. The current study confirms these findings but also that the VLPO receives only sparse input from the SPZ (Chou et al., 2002). Most people believe that DMH is a bridge between SPZ and VLPO (Phillips et al., 2013). Circadian information might be transmitted from the SCN to circuits based on DMH and SPZ to serve the sleep-wake transition.

The underlying circadian rhythms are generated by periodic activation of transcription by clock genes in the SCN (Reppert and Weaver, 2001). Konopka and Benzer identified a mutant gene named *period (per)* which affected the period length of circadian rhythmicity in the fruit fly (Konopka and Benzer, 1971). It provided the first evidence that a single gene has an impact on circadian rhythm. A number of additional clock gene families have been identified in flies and mammals later. These genes include *clock (clk)*, *cryptochrome (cry),* and *brain and muscle Arnt-like 1 (bmal1)* (Allada et al., 1998; Bunger et al., 2000; Vitaterna et al., 1994). The circadian rhythms are maintained intracellularly by interlocking positive- and negative-feedback control of transcription of these 4 clock genes. The Clock and Bmal1 proteins form a transcriptionally active heterodimer that promotes the transcription of *cry* and *per*. After translation of *cry* and *per* genes, the Cry and Per proteins form a complex and re-enter the nucleus to suppress the Clock and Bmal1, thereby forming the negative feedback loop. The RNA and protein levels of per and cry genes accumulate during organism's normally active state (wake period) and at the peak at sleep onset. Bmal1 and Clock proteins are accumulated during the time the organism is normally inactive (sleep period) (Young and Kay, 2001). In an attempt to establish the effects of clock genes on sleep behavior and circadian rhythm, mice with *Bmal1* homozygous knockout showed increases in total sleep time and sleep fragmentation (Laposky et al., 2005). The homozygous *Clock* mutant mice decreased around 2 hours of NREM sleep compared to wild type mice (Naylor et al., 2000). Interestingly, a dominant coding variation of cry1 gene in human causes delayed sleep phase disorder (DSPD) , a common form of insomnia in which sleep episodes are shifted to later times misaligned with the societal norm (Patke et al., 2017). Much literature provides the evidence of correlation between clock genes and sleep behavior. However, little is known about the mechanisms by which the clock genes drive rhythms in neural activity in the SCN. There are some hypotheses that need to be tested and verified, including changes in transcription and translation, direct phosphorylation, trafficking and distribution of ion channels in membrane of SCN neurons (Fogle et al., 2011; McDonald and Rosbash, 2001; O'Neill et al., 2008).

Sleep Homeostasis

In general, sleep homeostasis means an internal biochemical system that generates sleep pressure after a prolonged period of wakefulness. The sleep pressure is caused by the accumulation of sleep factors in daily life. The best-known sleep factor is adenosine. Adenosine

concentration increases in the basal forebrain during wakefulness consumes energy. Adenosine also inhibits wake active neurons to induce sleep (Porkka-Heiskanen et al., 1997). The arousal systems, such as the LC, TMN, and orexin neurons are inhibited by adenosine via the adenosine A1 receptors signaling pathway (Liu and Gao, 2007; Oishi et al., 2008; Pan et al., 1995).

Why do we usually feel sleepy when we are sick? Dr. Kruger provided a series fascinating research that related the immune system to sleep. The activation of immune systems increases cytokine levels. The cytokines, including Interleukin-1 and tumor necrosis factor, could regulate sleep (Krueger et al., 1984). These cytokines stimulate the hypothalamus to produce the growth hormone releasing hormone (GHRH) (Krueger et al., 1999). GHRH promotes NREM sleep via activation of GABAergic neurons in the preoptic area (Peterfi et al., 2010; Zhang et al., 1999). Thus, GHRH and cytokines are considered important sleep factors.

CHAPTER 2

Cell type-specific long range connections of basal forebrain circuit

Summary

The basal forebrain (BF) plays key roles in multiple brain functions, including sleep-wake regulation, attention, and learning/memory, but the long-range connections mediating these functions remain poorly characterized. Here we performed whole-brain mapping of both inputs and outputs of four BF cell types – cholinergic, glutamatergic, and parvalbumin-positive (PV+) and somatostatin-positive (SOM+) GABAergic neurons – in the mouse brain. Using rabies virus - mediated monosynaptic retrograde tracing to label the inputs and adeno-associated virus to trace axonal projections, we identified numerous brain areas connected to the BF. The inputs to different cell types were qualitatively similar, but the output projections showed marked differences. The connections to glutamatergic and SOM+ neurons were strongly reciprocal, while those to cholinergic and PV+ neurons were more unidirectional. These results reveal the long-range wiring diagram of the BF circuit with highly convergent inputs and divergent outputs and point to both functional commonality and specialization of different BF cell types.

Introduction

The BF has been implicated in a variety of brain functions such as arousal, attention, and plasticity (Bakin and Weinberger, 1996; Brown et al., 2012; Everitt and Robbins, 1997; Froemke et al., 2013; Hasselmo and Sarter, 2010; Jones, 2011; Lin et al., 2015; Saper et al., 2010; Sarter et al., 2001). The dysfunction or loss of BF cholinergic neurons is an important feature of Alzheimer's disease associated with cognitive impairment (Schliebs and Arendt, 2011; Whitehouse et al., 1982). In addition to forming extensive local synapses (Xu et al., 2015; Yang et al., 2014; Zaborszky and Duque, 2000), BF neurons receive inputs (Asanuma, 1989; Freund and Meskenaite, 1992; Grove, 1988a; Manns et al., 2001; Parent et al., 1988; Rye et al., 1984; Semba et al., 1988; Za´borsky and Cullinan, 1992) and send outputs (Cullinan and Zaborszky, 1991; Grove, 1988b; Jones and Cuello, 1989; Mesulam and Mufson, 1984; Paré and Smith, 1994) to many other brain areas. However, how these long-range connections contribute to BF functions remains unclear.

An important challenge in understanding the function of the BF circuit is its neuronal heterogeneity. There are three major cell types spatially intermingled in the BF: cholinergic, glutamatergic, and GABAergic (Semba, 2000).Selective lesion or pharmacological manipulation of the cholinergic system is well known to affect multiple brain functions (Wenk, 1997). For example, 192-IgG-saporin-mediated lesion of cholinergic neurons impaired the ability of rats to discriminate between signal and non-signal visual events in an attention task (McGaughy et al., 1996) and disrupted training-induced cortical map reorganization associated with motor learning (Conner et al., 2003). Glutamatergic and GABAergic BF neurons are also likely to serve important functions (Lin et al., 2015). For example, in recent studies the activity of non-cholinergic BF neurons was found to correlate with sustained attention (Hangya et al., 2015) or to encode reward and motivational salience information (Avila and Lin, 2014; Lin and Nicolelis, 2008; Nguyen and Lin, 2014), and optogenetic activation of PV+ GABAergic neurons was shown to regulate cortical gamma oscillations (Kim et al., 2015). In a study on sleep-wake control, cholinergic, glutamatergic, and PV+ neuron activity was found to promote wakefulness, while SOM+ neurons promoted sleep; these four cell types form extensive but highly specific local connections with each other for brain-state regulation (Xu et al., 2015). Thus, to understand the BF circuit function, it is crucial to map its inputs and outputs with cell-type specificity.

Most of the previous studies of BF long-range connections focused on specific regions connected to the BF, making it difficult to assess their whole-brain distribution. Recent advances in virus-assisted circuit tracing (Callaway and Luo, 2015; Huang and Zeng, 2013) and high-throughput imaging have greatly facilitated whole-brain mapping of long-range connectivity in a cell-type-specific manner (Oh et al., 2014; Osten and Margrie, 2013). In this study, we traced the long-range inputs and outputs of four genetically defined BF cell types. While the input distributions were similar across cell types, their output patterns showed striking differences. Our quantitative analysis of the whole-brain distributions of inputs and outputs for each BF cell type can serve as an anatomical blueprint for future studies of inter-regional pathways mediating BF functions.

Results

Four Cre mouse lines were used to target different BF subpopulations for virus-mediated circuit tracing: choline acetyltransferase (ChAT)-Cre for cholinergic neurons, vesicular glutamate transporter 2 (VGLUT2)-Cre for glutamatergic neurons, and PV-Cre and SOM-Cre mice for two subtypes of GABAergic neurons. These four Cre lines have been shown to label largely non-overlapping BF neuron populations with high specificity (Xu et al., 2015).

To identify the long-range inputs to each cell type, we used RV-mediated transsynaptic retrograde tracing, which has been shown to label monosynaptic inputs to selected starter cells with high specificity (Miyamichi et al., 2011; Wall et al., 2013; Watabe-Uchida et al., 2012; Wickersham et al., 2007). First, we expressed avian-specific retroviral receptor (TVA), enhanced green fluorescent protein (eGFP), and rabies glycoprotein (RG) specifically in each cell type by injecting two Cre-inducible AAV vectors (AAV2-EF1α-FLEX-eGFP-2a-TVA and AAV2-EF1α-FLEX-RG) into the BF of ChAT-, VGLUT2-, PV-, or SOM-Cre mice (Figure 1A). The expression of RG was highly cell type specific and not detected in wild-type mice not expressing Cre recombinase (Figure 1—figure supplement 1). Two to three weeks later, we injected a modified RV (rabiesΔG-tdTomato+EnvA) that only infects cells expressing TVA, requires RG to spread retrogradely to presynaptic cells (Figure 1—figure supplement 2), and contains the tdTomato transgene. After histological sectioning and fluorescence imaging, each sample was aligned to a reference atlas (Allen Mouse Brain Atlas, see Materials and methods) to facilitate 3D whole-brain visualization and quantitative comparison across brain samples (Figure 1C). The starter cells (expressing both tdTomato and eGFP) and the transsynaptically labeled presynaptic neurons (expressing tdTomato only) were identified manually, and their locations were registered in the reference atlas (Figure 1—figure supplement 3).

Brain samples were excluded from the analyses if very few input neurons (<200) were labeled in the whole brain. As noted in previous studies, due to the extremely efficient interaction between TVA and EnvA-pseudotyped rabies virus, the very low-level expression of TVA in non-Cre-expressing cells (not detectable based on fluorescent protein markers) allows the rabies virus to infect and label these cells with tdTomato at the injection site, independent of synaptic connections with starter cells (Beier et al., 2015; Menegas et al., 2015; Miyamichi et al., 2013; Ogawa et al., 2014; Pollak Dorocic et al., 2014; Wall et al., 2013; Watabe-Uchida et al., 2012; Weissbourd et al., 2014). However, this local contamination does not compromise the mapping of long-range inputs because RG (required for transsynaptic spread of RV) is not expressed in any non-Cre-expressing cells at sufficient levels for trans-complementation of rabiesΔG to allow transsynaptic spread of RV (Callaway and Luo, 2015; Miyamichi et al., 2013). To determine the spatial extent of the local contamination, we performed control experiments in the absence of RG and found very few non-specific labeling at >850 μm from the injection center (Figure 1—figure supplement 2D). Thus, presynaptic neurons were counted only in coronal sections outside of this range. While this procedure precludes identification of local inputs, synaptic interactions of the four cell types within the BF have been characterized electrophysiologically in a recent study (Xu et al., 2015). Another technical limitation of the study is that when the brain was removed for histological processing, the olfactory bulb was often damaged, which led

to a significant underestimation of labeling (both the input neurons and axon projections) in the olfactory bulb.

We found 900 – 14,631 (median 7002) tdTomato-labeled presynaptic neurons in each brain (n = 17), and the convergence index (ratio between the number of input cells and starter cells) ranged between 4.3 and 77.7 (Figure 1—figure supplement 4). Such variability is comparable to that found in other studies using similar methods (DeNardo et al., 2015; Miyamichi et al., 2011). The presynaptic neurons were predominantly ipsilateral to the starter population (<5% contralateral) but were distributed in a large number of brain areas (Figure 2, Figure 3, Video 1). Since the number of labeled neurons varied across brain samples, and there was no significant difference between the four cell types (P = 0.27, one-way ANOVA), we normalized the data in each area by the total number of labeled neurons in each brain. When the brain was divided into 12 major regions (Figure 3A), the striatum and hypothalamus provided the highest numbers of inputs, while few labeled neurons were found in the medulla or cerebellum (Figure 3A).

To facilitate data visualization at different levels of detail, we also used an interactive sunburst diagram (adapted from Allen Mouse Brain Atlas, http://www.brain-map.org/api/examples/examples/sunburst/) to represent the whole-brain distribution of inputs to each cell type (http://sleepcircuits.org/bf/). The brain structures are arranged hierarchically from inner to outer circles, and the size of each sector represents the percentage of input from the corresponding structure. The name of each structure and its input percentage can be read out by pointing the cursor, and each region of interest can be expanded with a mouse click.

When the input distribution was analyzed at a finer spatial scale (e.g., the 6th ring of the sunburst plot), the nucleus accumbens (DeNardo et al., 2015; Mesulam and Mufson, 1984; Miyamichi et al., 2011; Za´borsky and Cullinan, 1992), lateral hypothalamus (Cullinan and Zaborszky, 1991; Grove, 1988b; Mesulam and Mufson, 1984), and central nucleus of the amygdala (Grove, 1988b; Paré and Smith, 1994) were among the structures containing the highest numbers of input neurons (Figure 2). Interestingly, many close neighbors of these densely labeled structures (e.g., the basolateral nucleus of the amygdala, immediately adjacent to the central nucleus) showed very sparse or no labeling, indicating high spatial specificity of the long-range inputs. On the other hand, the input distributions were qualitatively similar between cell types, although with quantitative differences. For example, glutamatergic neurons received significantly more inputs from the lateral hypothalamus than the other cell types (P = 0.001, VGLUT2 vs. ChAT; P = 0.001, VGLUT2 vs. PV; P = 0.001, VGLUT2 vs. SOM;, one-way ANOVA and post-hoc Tukey's test), and PV+ neurons received more inputs from the nucleus accumbens (ACB) (P = 0.004, PV vs. ChAT; P = 0.003, PV vs. VGLUT2; P = 0.001, PV vs. SOM; one-way ANOVA and post-hoc Tukey's test).

To further verify the inputs revealed by RV-mediated retrograde tracing, we optogenetically tested the synaptic connections from the prefrontal cortex (PFC) and ACB (Figure 4). To verify the innervation from PFC to BF cholinergic neurons, we injected AAV (AAV-DJ-CaMKIIα-hChR2-eYFP) expressing the mammalian codon-optimized channelrhodopsin-2 (hChR2) fused with

enhanced yellow fluorescent protein (eYFP) in the orbital and agranular insular areas of the PFC (Figure 4—figure supplement 1) in ChAT-eGFP mice and made whole-cell voltage-clamp recordings from eGFP-labeled cholinergic neurons in acute BF slices (Figure 4A). Activating the ChR2-expressing axon terminals with blue light evoked excitatory responses in all recorded BF cholinergic neurons (n = 9, Figure 4B and C), confirming the input revealed with RV tracing. To confirm the innervation from ACB, we injected Cre-inducible AAV (AAV-DJ-EF1α-FLEX-ChR2-eYFP) expressing ChR2-eYFP in ACB of GAD2-Cre mice, made whole-cell current-clamp recordings from unlabeled postsynaptic BF neurons, and used single cell reverse-transcription PCR (RT-PCR) to identify the cell type. We found that all four BF cell types received inhibitory responses from the ACB (Figure 4D and E; ChAT+: 2 out 5 showed significant responses; VGLUT2+: 2/4; PV+: 3/3; SOM+: 4/8), which is consistent with the finding of an electron microscopic double-immunolabeling study performed in rats (Za´borsky and Cullinan, 1992).

We next mapped the output of each BF cell type. To label the axonal projections, we injected AAV with Cre-dependent expression of mCherry (Figure 1B) into the BF of ChAT-, VGLUT2-, PV- or SOM-Cre mice. Two to three weeks after injection, the brain tissues were processed, images were registered to the reference atlas, and labeled axons were detected (Figure 1C, see Materials and methods). After the injection site (identified by the existence of labeled cell bodies) and locations with known major fiber tracks were excluded, the projection to each brain area was quantified by the number of pixels occupied by the detected axons (Oh et al., 2014) (see Materials and methods).

Parallel to the broad distribution of inputs (Figure 3), we found that each BF cell type also projected to a large number of brain areas (Figure 5, Figure 6, Video 2, http://sleepcircuits.org/bf/, >95% ipsilateral). Among the 12 major brain subdivisions (Figure 6A), the hypothalamus, pallidum, and striatum received the heaviest BF projections (Grove, 1988a; Henny and Jones, 2006), while very few axons were detected in the medulla or cerebellum (Figure 6A). Analysis at finer scales revealed high spatial specificity of the projections. For example, while several cell types projected strongly to the lateral habenula (Figure 5), few axons were detected in the immediately adjacent but anatomically distinct medial habenula (Hikosaka, 2010). In addition to providing extensive inputs to the BF (Figure 2), the lateral hypothalamus was also a major recipient of BF projections (Figure 5), indicating a strong BF-hypothalamus loop that may be important for brain-state regulation (Brown et al., 2012; Jones, 2011; Saper et al., 2010). Importantly, whereas the input distributions were generally similar across BF cell types (Figure 2, Figure 3), the output patterns showed striking differences. For example, compared to the other cell types, the projection from cholinergic neurons was much stronger in the basolateral amygdala, hippocampus, and visual cortex but much weaker in the lateral hypothalamus, lateral habenula, and the ventral tegmental area (Figure 5). The different projection patterns among cell types are also apparent in the 3D whole-brain view (Figure 6B, Figure 6—source data 1).

To further compare the inputs and outputs between cell types, we averaged the spatial distributions across brain samples of each cell type and computed the correlation coefficient (CC) between cell types. For input distribution, the CCs between all cell types were high (Figure

7A), confirming their overall similarity observed earlier (Figure 2, Figure 3). On the other hand, when we computed the CCs between individual brain samples, we found higher CCs between samples of the same cell type (0.81 ± 0.04, s.e.m.) than of different cell types (0.70 ± 0.02, P = 0.01, t-test; Figure 7—figure supplement 1A). This indicates that despite the overall similarity, there were genuine differences between cell types that were beyond experimental variability.

For output distribution, the CCs between individual samples of the same cell type were also high (0.86 ± 0.05; Figure 7—figure supplement 1B), indicating reproducibility of the mapping. However, most of the CCs between cell types (Figure 7B, computed after averaging across samples of the same cell type) were much lower than those for input distribution. The two lowest CCs (ChAT+ vs. VGLUT2+ and PV+ neurons) reflect the fact that while the cholinergic neurons project strongly to structures within the cerebral cortex (including olfactory areas, isocortex, hippocampus, and cortical subplate) and weakly to the brain stem structures (thalamus, hypothalamus, and midbrain), glutamatergic and PV+ neurons (with output distributions highly similar to each other) showed complementary projection patterns (Figure 6).

Finally, we computed the CC between the input and output distributions of each cell type (Figure 7C). The highest CC was found for SOM+ neurons, reflecting their strong reciprocal connections with a number of brain structures, including the hypothalamus, striatum, pallidum, and olfactory areas (Figure 7D, lower right, Figure 7—source data 1. For glutamatergic neurons, the high CC reflects their strong reciprocal connections with the hypothalamus and striatum (Figure 7D, upper right). For cholinergic and PV+ GABAergic neurons, the CCs between input and output distributions were much lower, reflecting the facts that while both cell types receive strong input from the striatum, cholinergic neurons project strongly to the cerebral cortex, and PV+ neurons to the pallidum and hypothalamus (Figure 7D, upper and lower left).

Discussion

Using virus-mediated circuit mapping, we have characterized the whole-brain distributions of BF long-range connections, available in an open-access online database (http://sleepcircuits.org/bf/). Our experiments confirmed many previously demonstrated connections, but with cell-type specificity and quantitative analyses at multiple spatial scales. For example, we found that cortical inputs (Mesulam and Mufson, 1984) to all four BF cell types originate primarily from the agranular insular and orbital areas of the prefrontal cortex (Figure 2). While a previous ultrastructural study failed to detect convincing synaptic contact between prefrontal axons and BF cholinergic neurons (Zaborszky et al., 1997), our RV-mediated transsynaptic tracing demonstrated extensive monosynaptic innervation, which was also validated by electrophysiological recordings (Figure 4B and C). These findings have important implications on how the prefrontal cortex may exert top-down control of neural processing through its projection to the BF (Sarter et al., 2001). A recent study showed that cholinergic neurons in the BF are strongly activated by reinforcement signals during an auditory detection task (Hangya et al., 2015). Our whole-brain mapping of their inputs provides a list of candidate neurons through which the reinforcement signals are conveyed to the BF cholinergic neurons.

Regarding the outputs, we found striking differences across cell types (Figure 6). A recent study has shown that cholinergic, glutamatergic, and PV+ neurons all promote wakefulness, while SOM+ neurons promote sleep (Xu et al., 2015). The distinct projection patterns between cholinergic and glutamatergic/PV+ neurons (Figure 6) suggest that they preferentially regulate different brain functions during wakeful states. In a recent study, optogenetic activation of BF PV+ neurons was shown to enhance cortical gamma band oscillations (Kim et al., 2015). In addition to direct projections to the cortex, our study showed extensive subcortical projections of PV neurons, which may also contribute to the regulation of cortical gamma oscillations. The output distribution of SOM+ neurons, on the other hand, was highly correlated with the input distributions of all BF cell types (Figure 7C, bottom row); the broad GABAergic inhibition of these input areas by SOM+ neurons may be important for the sleep-promoting effect. Thus, while the highly convergent inputs from multiple brain areas allow a variety of sensory, motor, cognitive, and emotional signals to be integrated within the BF, the distinct projections by different cell types may enhance the versatility of the BF in coordinating diverse functions of multiple brain networks.

Materials and Methods

Virus preparation

Transsynaptic retrograde tracing

To construct AAV2-EF1α-FLEX-eGFP-2a-TVA and AAV2-EF1α-FLEX-RG, TVA and eGFP linked by the 2A 'self-cleaving' peptide or rabies glycoprotein was respectively cloned into pAAV-MCS (Stratagene, La Jolla, CA) in an antisense direction flanked by a pair of canonical loxP sites and a pair of lox2272 sites. AAV particles (AAV2/2) were produced by co-transfection of packaging plasmids into HEK293T cells, and cell lysates were fractionated by iodixanol gradient ultracentrifugation. Viral particles were further purified from the crude fraction by heparin affinity column (HiTrap Heparin HP Columns; GE Healthcare, Pittsburgh, PA), desalted and concentrated with Amicon Ultra Centrifugal Filter (100 K, Millipore, Bellerica, MA). The genomic titer of AAV2-EF1α-FLEX-eGFP-2a-TVA (4.4×10^{13} gc/ml) and AAV2-EF1α-FLEX-RG (2.2×10^{12} gc/ml) was estimated by quantitative PCR. eGFP-2a-TVA and rabies glycoprotein were subcloned from the AAV-TRE-HTG plasmid from L. Luo.

RV-ΔG-tdTomato was amplified in B7GG cells and pseudotyped using BHK-EnvA cells. EnvA pseudotyped rabies virus was titered (1.5×10^9 IU/ml) by infecting the 293T-TVA8000 (Narayan et al., 2003) cell line with serial dilutions of the stock virus. RV-ΔG-tdTomato was a gift from B. Lim. B7GG cells, BHK-EnvA cells (Wickersham et al., 2007), and 293T-TVA8000 cells were gifts from E. Callaway.

Anterograde axon tracing

AAV2-EF1α-FLEX-mCherry was purchased from the UNC Vector Core (Chapel Hill, NC) and the titer was estimated to be ~10^{12} gc/ml.

Surgery and viral injections

All experimental procedures were approved by the Animal Care and Use Committee at the University of California, Berkeley. For the current study, we targeted the caudal portion of the BF (including the horizontal limb of the diagonal band of Broca, magnocellular preoptic nucleus, and substantia innominata) rather than the rostral nuclei (medial septum and the vertical limb of the diagonal band of Broca). For virus injection, adult (>P40) Chattm2(cre)Lowl (ChAT-Cre, JAX#006410), Slc17a6tm2(cre)Lowl (Vglut2-Cre, JAX#016963), Pvalbtm1(cre)Arbr (PV-Cre, JAX#008069), and Ssttm2.1(cre)Zjh (SOM-Cre, JAX#013044) mice were anesthetized with ~1.5% isoflurane in oxygen (flow rate of 1L/min). A craniotomy (~0.5 mm diameter) was made at 0.1 mm posterior to bregma, 1.3 mm lateral to midline. For anterograde axon tracing, 300–400 nL of AAV (serotype 2) expressing Cre-dependent mCherry (AAV2-EF1α-FLEX-mCherry) was stereotactically injected into the BF (5.2 mm from brain surface) using Nanoject II (Drummond Scientific, Broomall, PA) via a micro pipette. The following steps were taken to minimize virus leaking into the injection track: (1) The pipette opening was minimized (<20 μm); (2) The

injector was mounted onto a motorized manipulator to ensure slow and smooth retraction; (3) The injection started 5 min after pipette insertion, and multiple 23 or 40 nl injections (13 nl/s) were made at 15–30 s intervals. The pipette was retracted 10 min after injection.

For transsynaptic retrograde tracing, 200–300 nl of helper AAV (AAV2-EF1α-FLEX-eGFP-2a-TVA and AAV2-EF1α-FLEX-RG mixed at 1:1 ratio of viral particles) was injected into the BF using the same procedure as described above. Two to three weeks after helper AAV injection, RVΔG-tdTomato+EnvA was injected into the same location. To further ensure localized virus expression, the helper AAV injection pipette was tilted at 20 degrees from vertical while RV injection pipette was inserted vertically in the majority of experiments.

Tissue processing

Brain tissue was processed according to standard procedures. In brief, two to three weeks after AAV injection (for anterograde tracing) or one week after RV injection (for retrograde tracing), mice were deeply anesthetized with isoflurane and immediately perfused intracardially with ~15 ml of phosphate-buffered saline (PBS) (pH 7.2) followed by ~15 ml of 4% paraformaldehyde (PFA) in PBS. Brain tissue was carefully removed, post-fixed in 4% PFA in PBS at 4°C overnight, dehydrated in 30% sucrose in PBS for 48 hr, and embedded in Tissue Freezing Medium (Triangle Biomedical Sciences, Cincinnati, OH). Brains were cut in 30 or 50 µm coronal sections using a cryostat (Thermo Scientific, Waltham, MA) and mounted with VECTASHIELD mounting medium with DAPI (Vector Laboratories, Burlingame, CA) or DAPI Fluoromount-G (Southern Biotech, Birmingham, AL). One out of every three sections were imaged using 20X/0.75 objective in a high-throughput slide scanner (Nanozoomer-2.0RS, Hamamatsu, Japan) for further processing. We also imaged selected brain regions (Figures 2 and 3) using a Zeiss (Germany) inverted AxioObserver Z1 fully motorized microscope with LSM 710 confocal scanhead, 10X/0.3 EC Plan Neofluar M277 objective or a 20X/0.8 Plan Apochromat M27 objective.

Immunostaining

To check for cell-type specific expression of rabies glycoprotein, tdTomato transgenic reporter mice (JAX#007914) were crossed to Cre-transgenic mice for each cell type and double transgenic offspring were injected with AAV2-EF1α-FLEX-RG. Alternatively, Cre-transgenic mice were injected with AAV2-EF1α-FLEX-mCherry and AAV2-EF1α-FLEX-RG.

After making coronal sections, brain slices were washed in PBS (3 x 10 min., room temperature), blocked with mouse IgG blocking reagent (Mouse on Mouse (M.O.M.) Kit, Vector Laboratories, Burlingame, CA) for 2 hr at room temperature, incubated with mouse anti-rabies glycoprotein (clone 24-3F-10, EMD Millipore, Billerica, MA) with M.O.M. protein concentrate in PBST (PBS + 0.3% Triton-X100) for 18 hr at room temperature, washed in PBST (3 x 20 min., room temperature), incubated with Alexa-Fluor 488 or 647 donkey anti-mouse (ThermoFisher Scientific, Waltham, MA) with M.O.M protein concentrate in PBST for 3 hr at room temperature, and finally washed in PBST (3 x 10 min, room temperature) prior to mounting the slides.

3D reconstruction and quantification

A software package was developed in Matlab to analyze the digitized brain images. The analysis software consists of three modules: image registration, signal detection, and quantification/visualization.

Registration module

The registration module is a reference point-based image alignment software used to align images of brain sections to the Allen Mouse Brain Atlas for further quantification and 3D reconstruction. First, we manually selected a set of reference points in both the atlas and the brain image. The module then applied several geometric transformations (translation, rotation and scaling) of the brain section to optimize the match of the reference points between the brain image and the atlas. Since histological sectioning can sometimes cause tissue compression, we allowed the scaling factors along the dorsal-ventral and medial-lateral axes to be optimized independently. Following the transformation, the match between the image and the atlas was inspected, and further adjustments were made manually if necessary. The main purpose of the manual adjustment was to correct errors generated by the registration procedure due the imperfect brain slice preparations, and it was mostly performed by research assistants not involved in the research design and unaware of the final conclusion of the study.

Detection module

The detection module has two independent sub-modules designed for counting RV-labeled cells and detecting axons, respectively. The cell counting module records the position of manually identified tdTomato-labeled neurons in each digitized brain sections image.

For axon detection, the ridge detection method was used (http://en.wikipedia.org/wiki/Ridge_detection). The following steps were taken to maximize the detection accuracy: (1) Image ridges were computed across multiple scales to extract all possible axon-like signals from each image. In the resulting binary 'ridge image', the number of pixels occupied by each detected axon depends on the length but not the thickness of the axon. In addition to valid axons, the ridge image also contains many noise pixels. (2) To remove the noise pixels due to the general background in the fluorescence image, we set a threshold based on the intensity distribution of the original image, and use this as a mask to remove the noise pixels in the ridge image obtained from step (1). (3) To remove the discrete noise pixels with fluorescence intensities higher than the general background (thus not removed by step 2), we first identified pixels that are spatially contiguous in the ridge image, computed the size of each contiguous region, and removed the regions below a threshold size. Steps 2 and 3 were repeated until satisfactory detection results were achieved. (4) The results were then visually inspected and the remaining noise pixels, which were mostly artifacts introduced during brain tissue processing, were rejected manually.

Quantification/visualization module

After detection and registration, signals were quantified across the whole brain and projected to the 3D reference atlas for better visualization. The 3D viewer plug-in of the ImageJ software was used to animate the final 3D model.

The atlas, 3D reference mouse brain, quantification ontology, and layouts for sunburst plot were obtained from the open online resource of Allen Institute for Brain Science, licensed under the Apache License (Version 2.0). Since the number of labeled neurons or axons varied across brains, the input from each region was quantified by dividing the number of labeled neurons found in that region by the total number of labeled neurons detected >850 μm from the injection site (see Figure 1—figure supplement 2). The output (axon projection) to each region was quantified as the number of pixels occupied by detected axons in the cleaned ridge image (Oh et al., 2014) (see Detection module above) divided by the total number of axon-occupied pixels found in the entire brain (after excluding the injection site and locations with known major fiber tracks).

Starter cell mapping

Starter cells were manually identified from the colocalization of tdTomato and eGFP signals using Nanozoomer images scanned at multiple focal planes. The starter cells were marked using the Cell Counter ImageJ plug-in, and registered to the Allen Brain Reference Atlas as described above. A starter cell heat map was generated in Python by calculating the normalized starter cell density for all samples from each cell type and applying bicubic interpolation. For each coronal section image, the cell density was binned from an anterior-posterior range of 0.24 mm, centered at the listed brain slice coordinate (Figure 1—figure supplement 3).

Slice recording

To validate the synaptic input from the prefrontal cortex to BF cholinergic neurons (as shown by RV-mediated input tracing), ChR2 was expressed in excitatory neurons in the prefrontal cortex of ChAT-eGFP mice (JAX#007902, P16-P18) by injecting ~500 nl of AAV-DJ-CaMKIIα-hChR2-eYFP (~10^{13} gc/ml, Stanford Gene Vector and Virus Core, Stanford, CA) into the orbital and agranular insular areas of the PFC (2.0 mm anterior to bregma, 1.5 mm lateral, 2.0 mm from brain surface) and recording from eGFP+ BF neurons. To validate the synaptic input from ACB, Cre-inducible ChR2-eYFP was expressed in GAD2-Cre mice (JAX#010802, P16-P18) by injecting 300–400 nl of AAV-DJ-EF1α-FLEX-ChR2-eYFP (~10^{13} gc/ml, Stanford Gene Vector and Virus Core, Stanford, CA) into the ACB (1.5 mm anterior to bregma, 0.8 mm lateral, 3.6 mm from brain surface) and recordings were made (one week after virus injection) from unlabeled BF neurons, which were identified after each recording via single-cell gene-expression analysis. Slice preparation, recording procedure, and single-cell gene-expression analysis were the same as described in a recent study (Xu et al., 2015).

Figures

Figure 1.

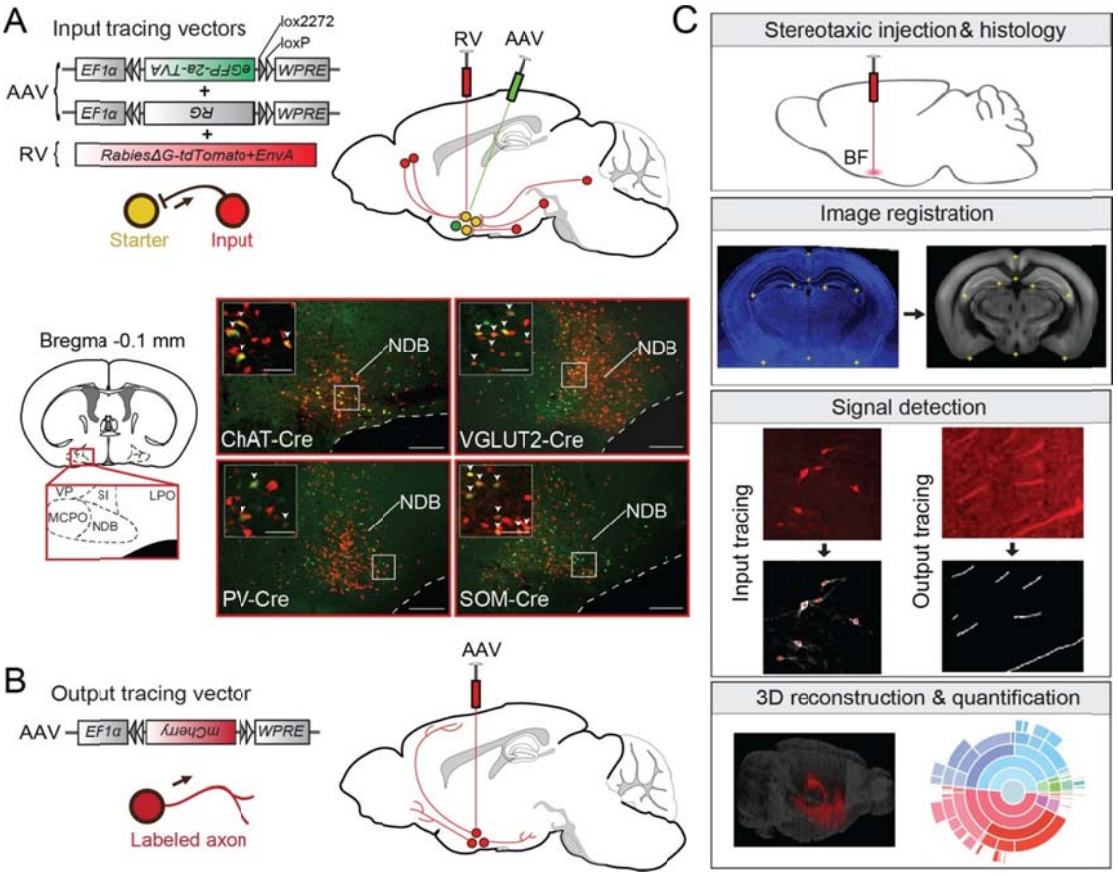

Figure 1: **Experimental and analysis procedures for cell-type-specific circuit tracing.**
A) RVmediated transsynaptic retrograde tracing of BF inputs. Upper panel, viral vectors and injection procedure. Lower panel, fluorescence images of BF in the region of the NDB (red box in coronal diagram) in ChAT-, VGLUT2-, PV-, and SOM-Cre mice. Scale bar, 200 µm. Inset, enlarged view of the region in white box showing starter cells (yellow, expressing both eGFP and tdTomato, indicated by white arrowheads). Scale bar, 50 µm. NDB, diagonal band nucleus; SIB, substantia innominata, basal part; MCPO, magnocellular preoptic nucleus; VP, ventral pallidum; LPO, lateral preoptic area. **B)** Viral vector and injection procedure for tracing BF axonal projections. **C)** Flow chart showing the main steps in data generation and processing.

Figure 2.

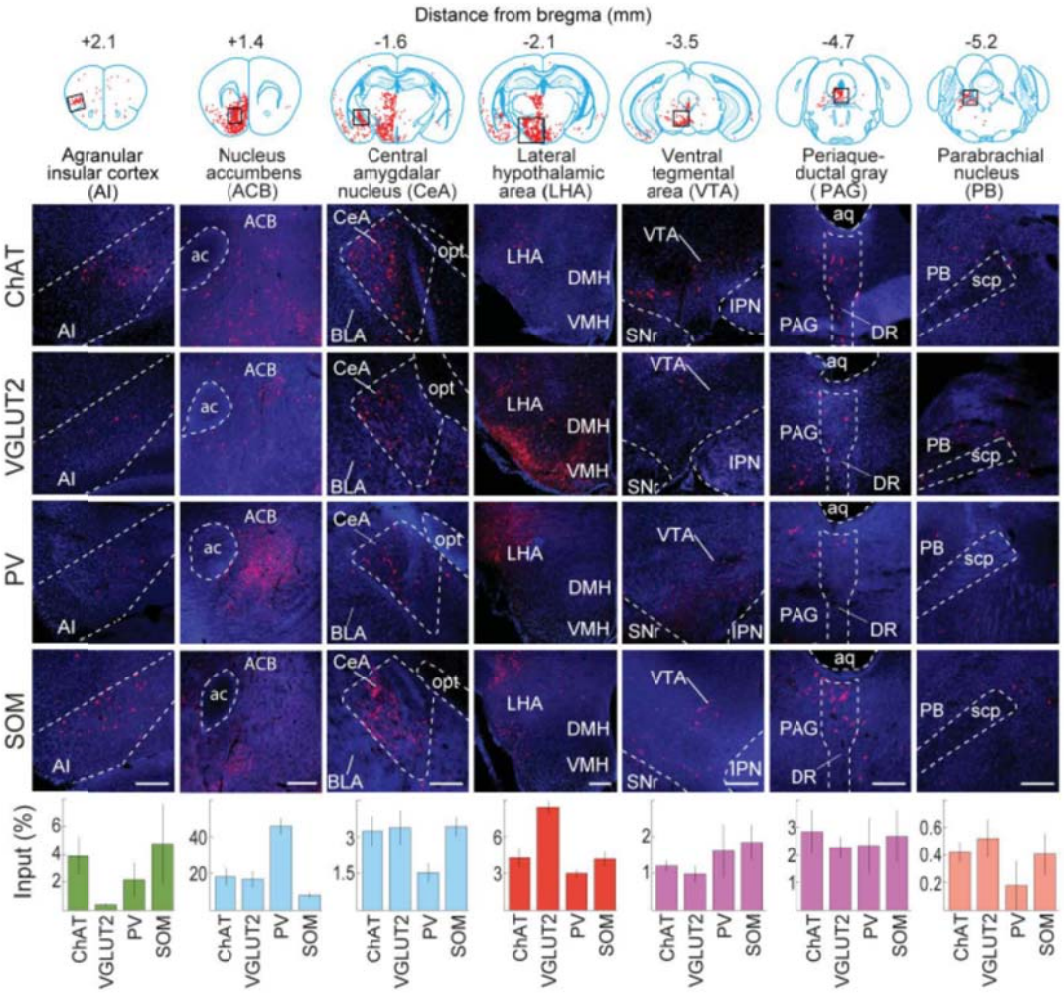

Figure 2: Inputs to each BF cell type from selected brain regions.
Examples of RV-labeled input neurons to each of the four BF cell types in seven selected brain structures (black box in each coronal diagram). Scale bar, 200 µm. In each coronal diagram, RV-labeled neurons detected in all four brain samples are indicated by red dots. Bottom panel, mean percentage of input neurons in each brain structure for the four BF cell types. Error bar, ± s.e.m. Bar color indicates which of the 12 regions the given brain structure belongs to as depicted in Figure 3. ac, anterior commissure; aq, cerebral aqueduct; BLA, basolateral amygdalar nucleus; DMH, dorsomedial nucleus of the hypothalamus; DR, dorsal nucleus raphe; IPN, interpeduncular nucleus; opt, optic tract; scp, superior cerebellar peduncles; SNr, substantia nigra reticularis; VMH, ventromedial hypothalamic nucleus.

Figure 3.

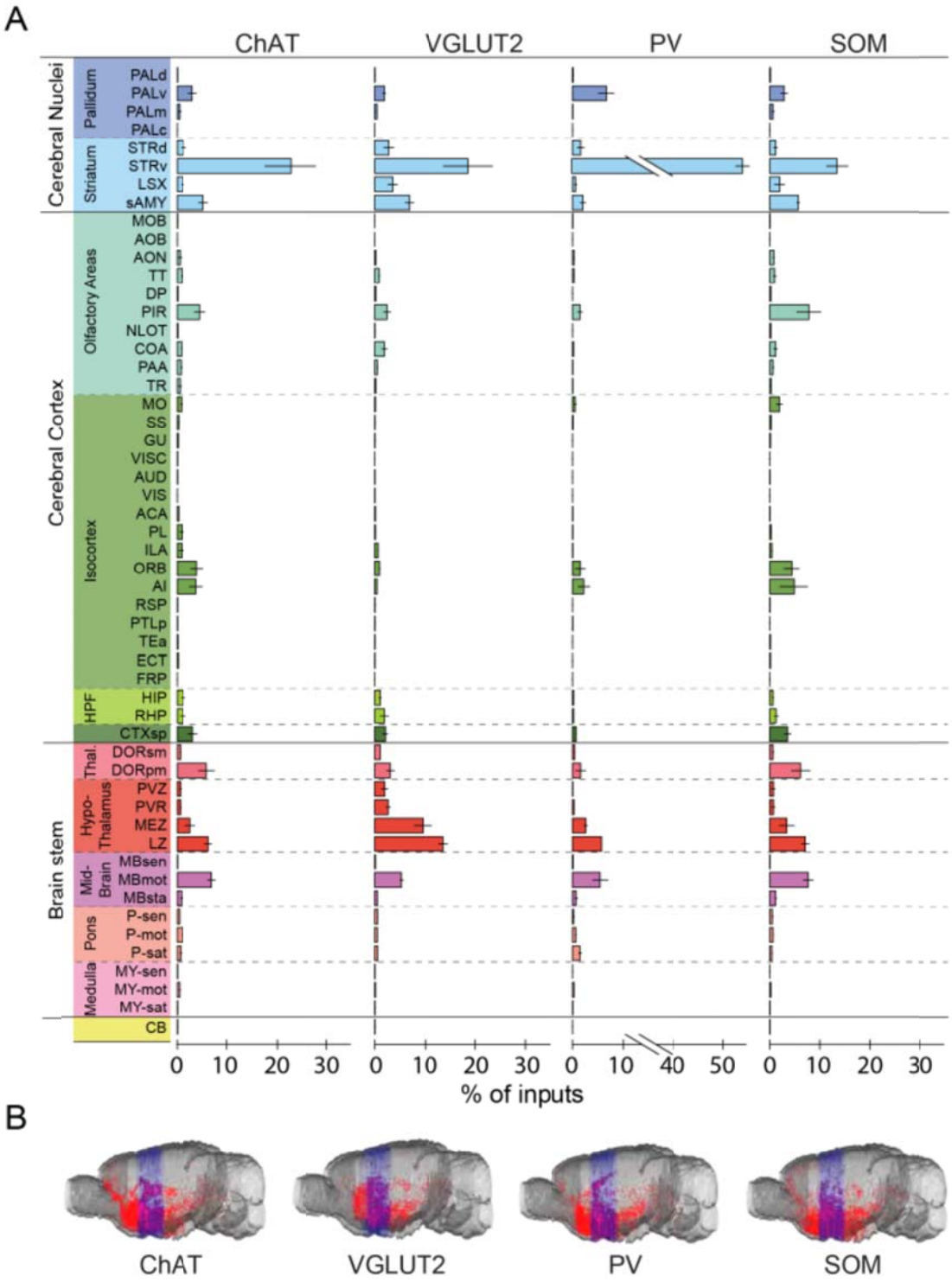
A
ChAT
VGLUT2
PV
SOM
Cerebral Nuclei
Pallidum
PALd
PALv
PALm
PALc
Striatum
STRd
STRv
LSX
sAMY
Cerebral Cortex
Olfactory Areas
MOB
AOB
AON
TT
DP
PIR
NLOT
COA
PAA
TR
Isocortex
MO
SS
GU
VISC
AUD
VIS
ACA
PL
ILA
ORB
AI
RSP
PTLp
TEa
ECT
FRP
HPF
HIP
RHP
CTXsp
Brain stem
Thal.
DORsm
DORpm
Hypo-Thalamus
PVZ
PVR
MEZ
LZ
Mid-Brain
MBsen
MBmot
MBsta
Pons
P-sen
P-mot
P-sat
Medulla
MY-sen
MY-mot
MY-sat
CB
0 10 20 30
0 10 20 30
0 10 40 50
0 10 20 30
% of inputs
B
ChAT
VGLUT2
PV
SOM

Figure 3: Whole-brain distributions of inputs to the four BF cell types.
A) Percentages of retrogradely labeled input neurons in 53 brain areas (ChAT, n = 5 mice; VGLUT2, n = 5; PV, n = 3; SOM, n = 4). Brain areas are grouped into 12 generalized, colorcoded brain structures. HPF, hippocampal formation. Abbreviations of the 53 brain areas and their percentages of inputs are listed in Figure 3 – source data 1. Error bar, ± s.e.m. Since labeled neurons in coronal sections near the injection site were excluded from analysis (see Figure 1 – figure supplement 2), inputs from the pallidum are likely to be underestimated. **B)** Whole-brain 3D reconstruction of the inputs to the four BF cell types. The blue-shaded area denotes the region excluded for analysis due to potential local contamination (see Figure 1 – figure supplement 2)

Figure 4.

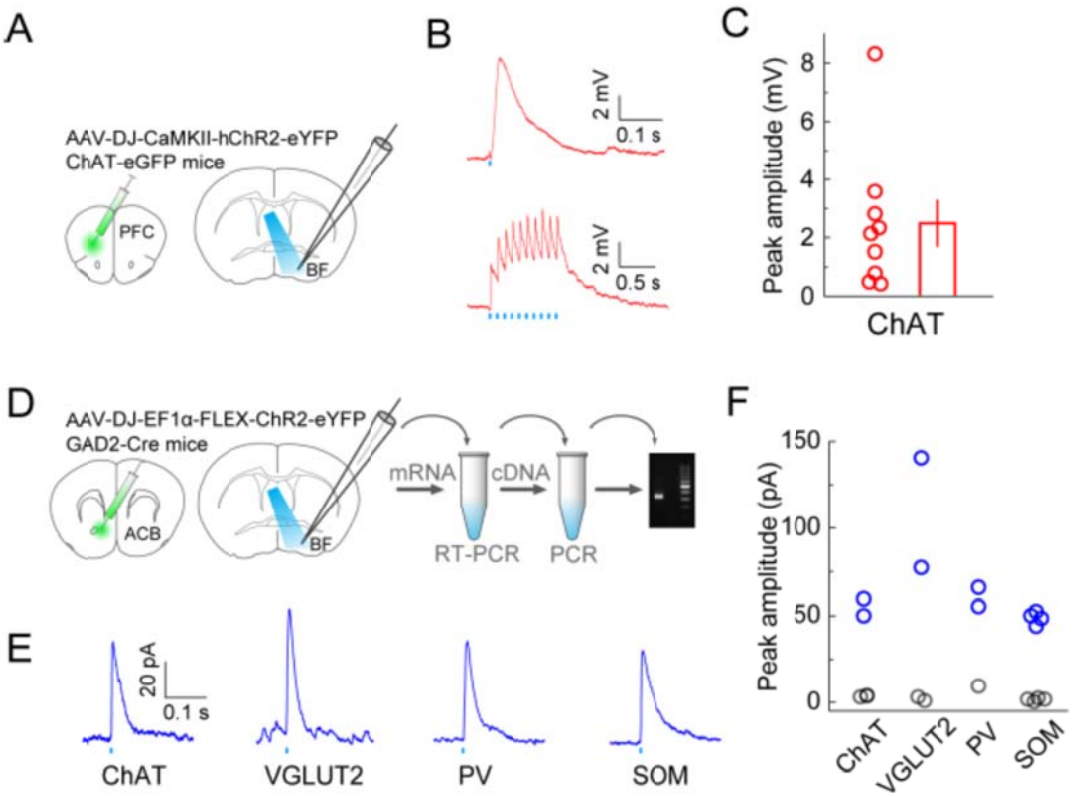

Figure 4: Optogenetic characterization of monosynaptic inputs to the BF from PFC and ACB. **A)** Schematic of experiment. ChR2 was expressed in excitatory neurons in the prefrontal cortex of ChAT-eGFP mice by injecting AAV-DJ-CaMKIIα-hChR2-eYFP. Coronal slices of the BF were used for recording experiments. **B)** Excitatory postsynaptic potentials recorded from ChAT+ neurons (under whole-cell current clamp) evoked by blue-light activation of the prefrontal cortical axons. Upper, response to a single light pulse (5 ms) in an example ChAT+ neuron; lower, responses to 10 pulses at 10 Hz recorded from a different ChAT+ neuron. **C)** Summary of the peak amplitude of the response to a single light pulse. Each circle represents data from one BF ChAT+ neuron (*n* = 9 neurons from 2 mice). Bar, mean ± s.e.m. **D)** Diagram illustrates virus injection site in the ACB and recording site in the BF. AAV-DJ-EF1α-FLEX ChR2-eYFP was injected into the ACB of GAD2-Cre mice and whole-cell voltage-clamp recordings (clamped at 0 volts) were made from BF neurons. Single-cell gene-expression analysis was performed after each recording session to identify the cell type of each recorded neuron. **E)** Example traces of laser-evoked responses in the four BF cell types. **F)** Summary of the peak current amplitude of each neuron's response (ChAT+, *n* = 5 neurons from 5 mice; VGLUT2+, *n* = 4 neurons from 4 mice; PV+, *n* = 3 neurons from 3 mice; SOM+, *n* = 8 neurons from 4 mice). Gray indicates no significant response.

Figure 5.

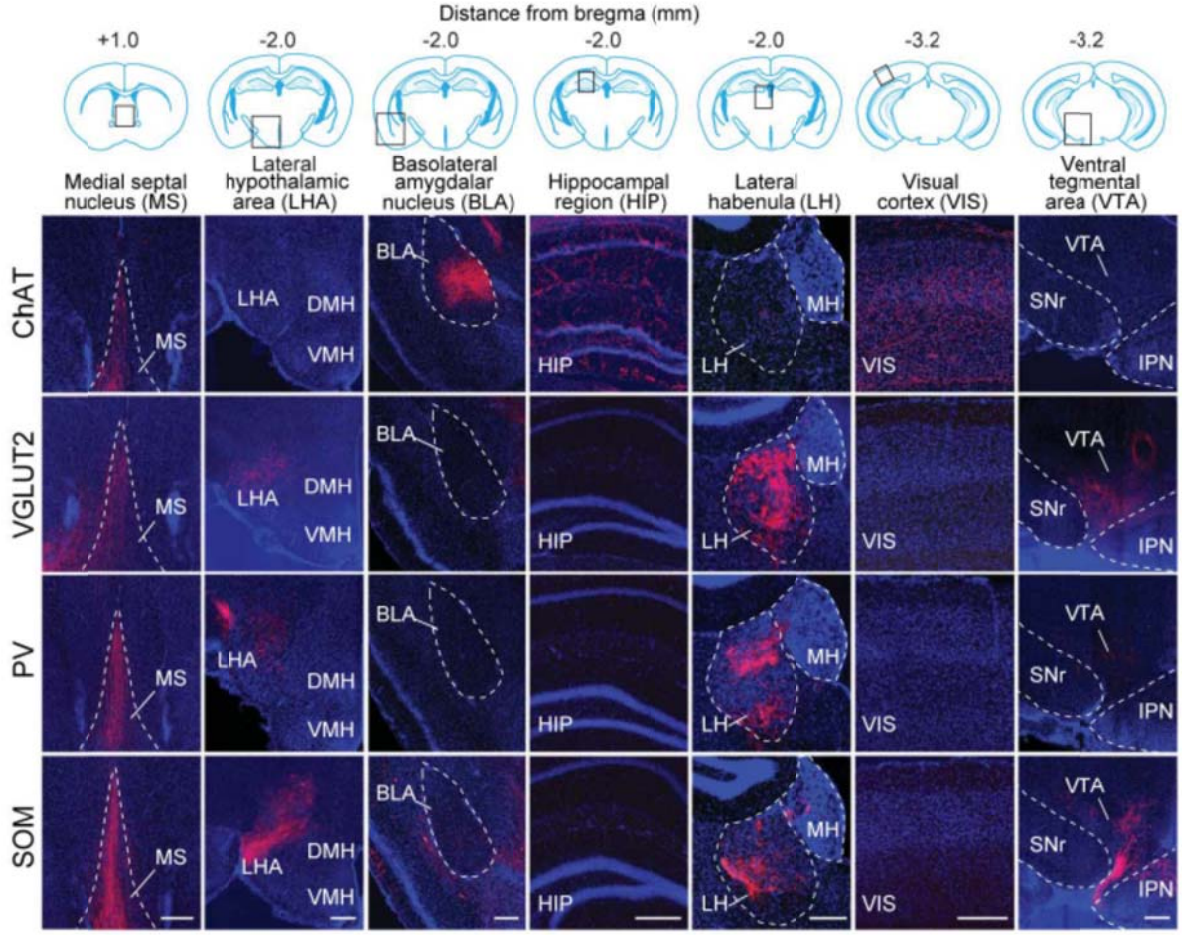

Figure 5: Axon projections of each BF cell type to selected brain regions.
Examples of axon projections from each of the four BF cell types to seven selected brain structures (black box in each coronal diagram). Scale bar, 250 µm. DMH, dorsomedial nucleus of the hypothalamus; IPN, interpeduncular nucleus; MH, medial habenula; SNr, substantia nigra reticularis; VMH, ventromedial hypothalamic nucleus.

Figure 6.

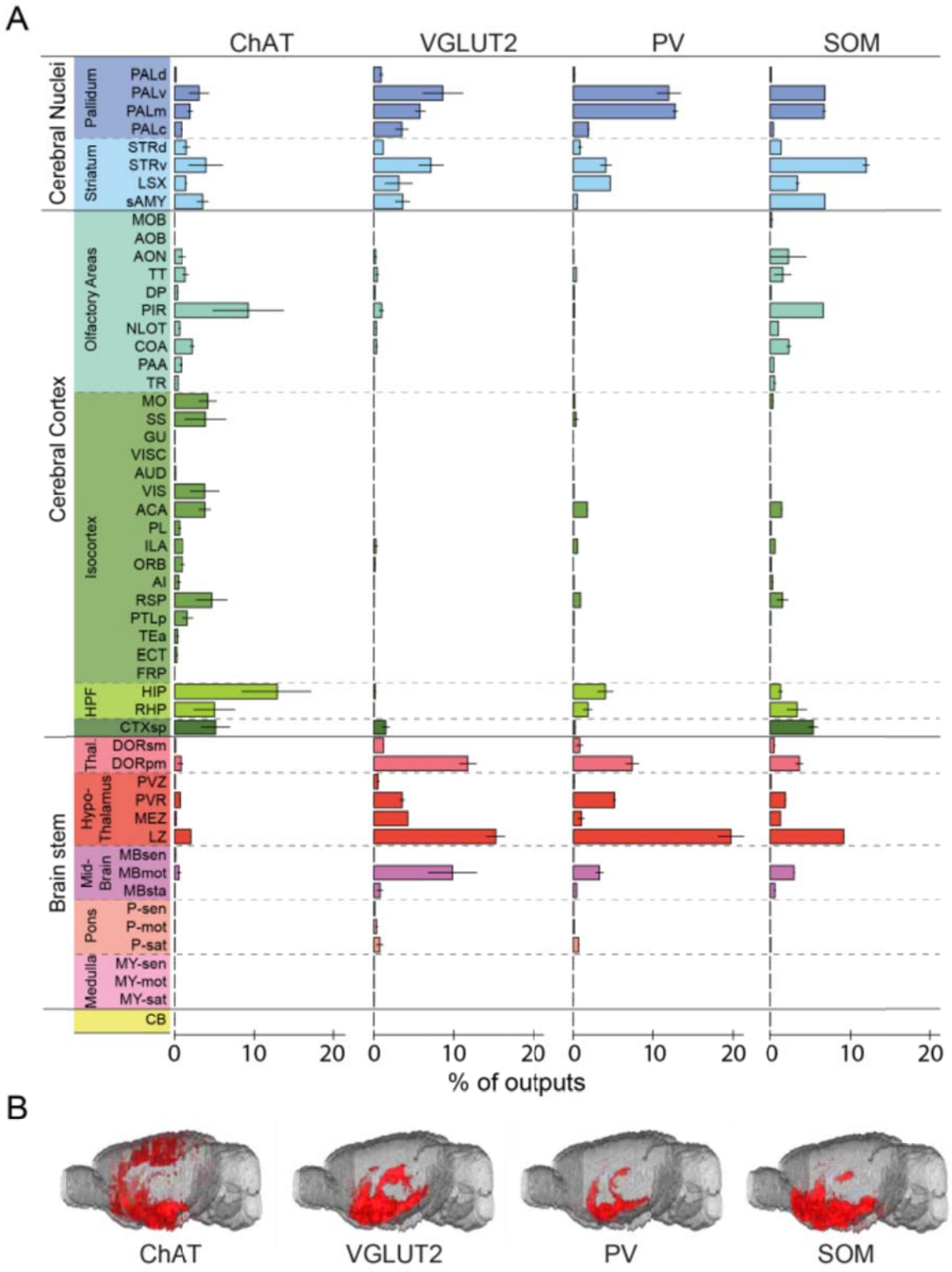
A
ChAT
VGLUT2
PV
SOM
Cerebral Nuclei
Pallidum
PALd
PALv
PALm
PALc
Striatum
STRd
STRv
LSX
sAMY
Cerebral Cortex
Olfactory Areas
MOB
AOB
AON
TT
DP
PIR
NLOT
COA
PAA
TR
Isocortex
MO
SS
GU
VISC
AUD
VIS
ACA
PL
ILA
ORB
AI
RSP
PTLp
TEa
ECT
FRP
HPF
HIP
RHP
CTXsp
Brain stem
Thal.
DORsm
DORpm
Hypo-Thalamus
PVZ
PVR
MEZ
LZ
Mid-Brain
MBsen
MBmot
MBsta
Pons
P-sen
P-mot
P-sat
Medulla
MY-sen
MY-mot
MY-sat
CB
0
10
20
% of outputs
B
ChAT
VGLUT2
PV
SOM

Figure 6: Whole-brain distributions of axonal projections from the four BF cell types.
A) Percentages of labeled axons in 53 brain areas (ChAT, n = 3 mice; VGLUT2, n = 3; PV, n = 3; SOM, n = 3). Error bar, ± s.e.m. Abbreviations of the 53 brain areas and their percentages of inputs are listed in Figure 6 – source data 1. **B)** Whole-brain 3D reconstruction of axon projections from each of the four BF cell types. Note that although VGLUT2+ and PV+ neuron projections showed the similar spatial distribution, there were fewer labeled axons from PV+ than VGLUT2+ neurons

Figure 7.

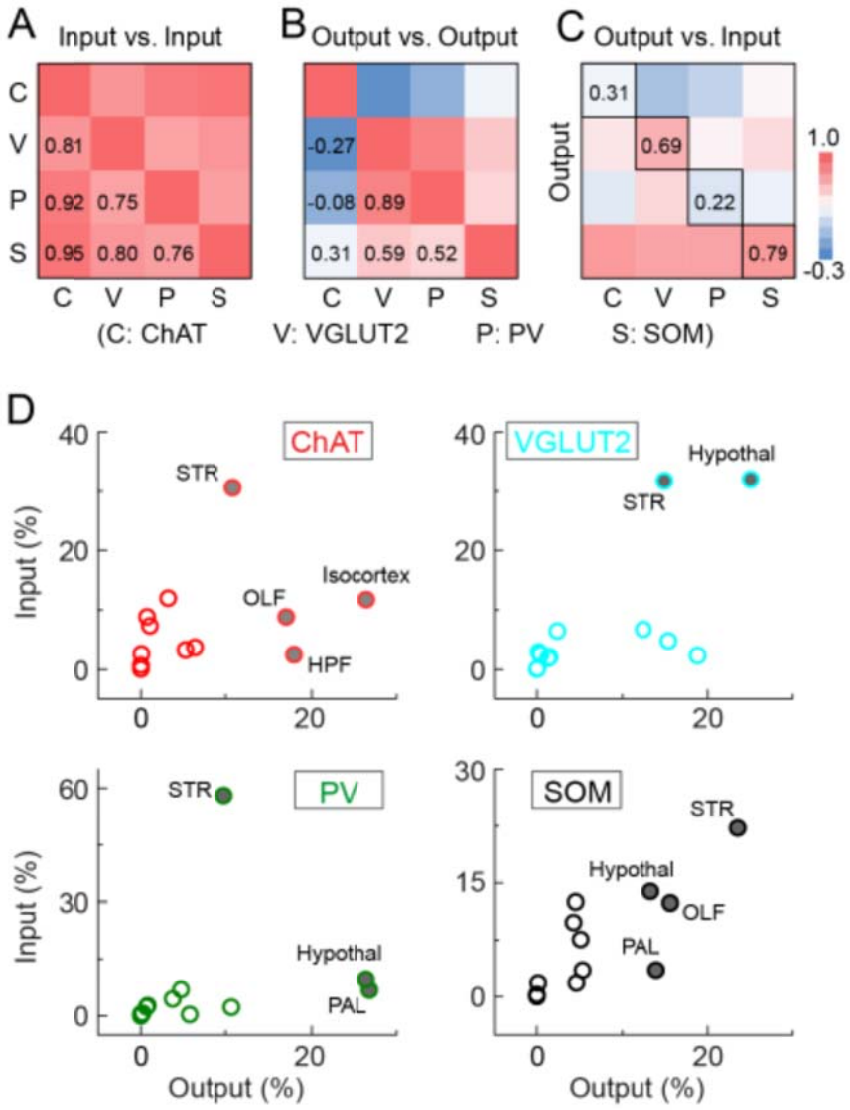

Figure 7: Comparison of input and output distributions.
A) Matrix of correlation coefficients (CCs) between input distributions of each pair of cell types. **B)** Similar to **A**, for output distributions. **C)** CCs between input and output distributions. All CCs were computed at the spatial scale of the 12 major brain subdivisions (Figure 7 – source data 1). **D)** Percentage of input vs. percentage of output in each region, for each of the four BF cell types. Filled circles, strongly connected brain regions contributing to the high CCs for glutamatergic and SOM+ neurons and low CCs for cholinergic and PV+ neurons in **C**.

Supplemental Figures

Figure 1 – figure supplement 1.

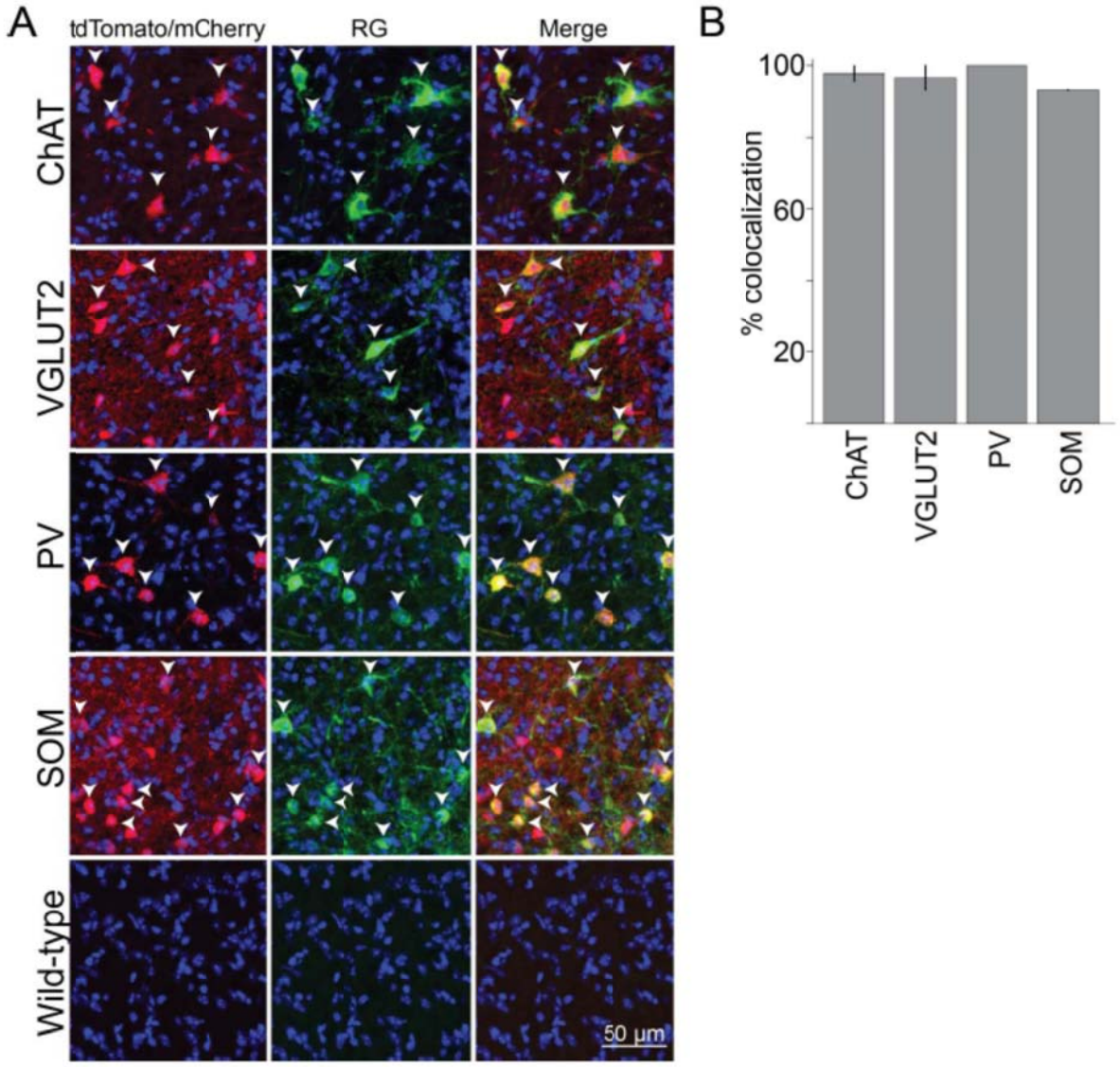

Figure 1 – figure supplement 1: Cell-type specificity of Cre-dependent rabies glycoprotein expression.

A) Colocalization of rabies glycoprotein immunostaining with Cre expression (indicated by tdTomato or mCherry reporters) in each of the four Cre lines. White arrowheads indicate cells with colocalization. No rabies glycoprotein expression was detected when injected into wild type mice. **B)** Percentage of rabies glycoprotein expressing cells that are positive for tdTomato or mCherry, averaged across brain samples. Error bar, ± standard deviation (91 ChAT cells; 89 VGLUT2 cells; 70 PV cells; 100 SOM cells; n = 2 mice per line).

Figure 1 – figure supplement 2.

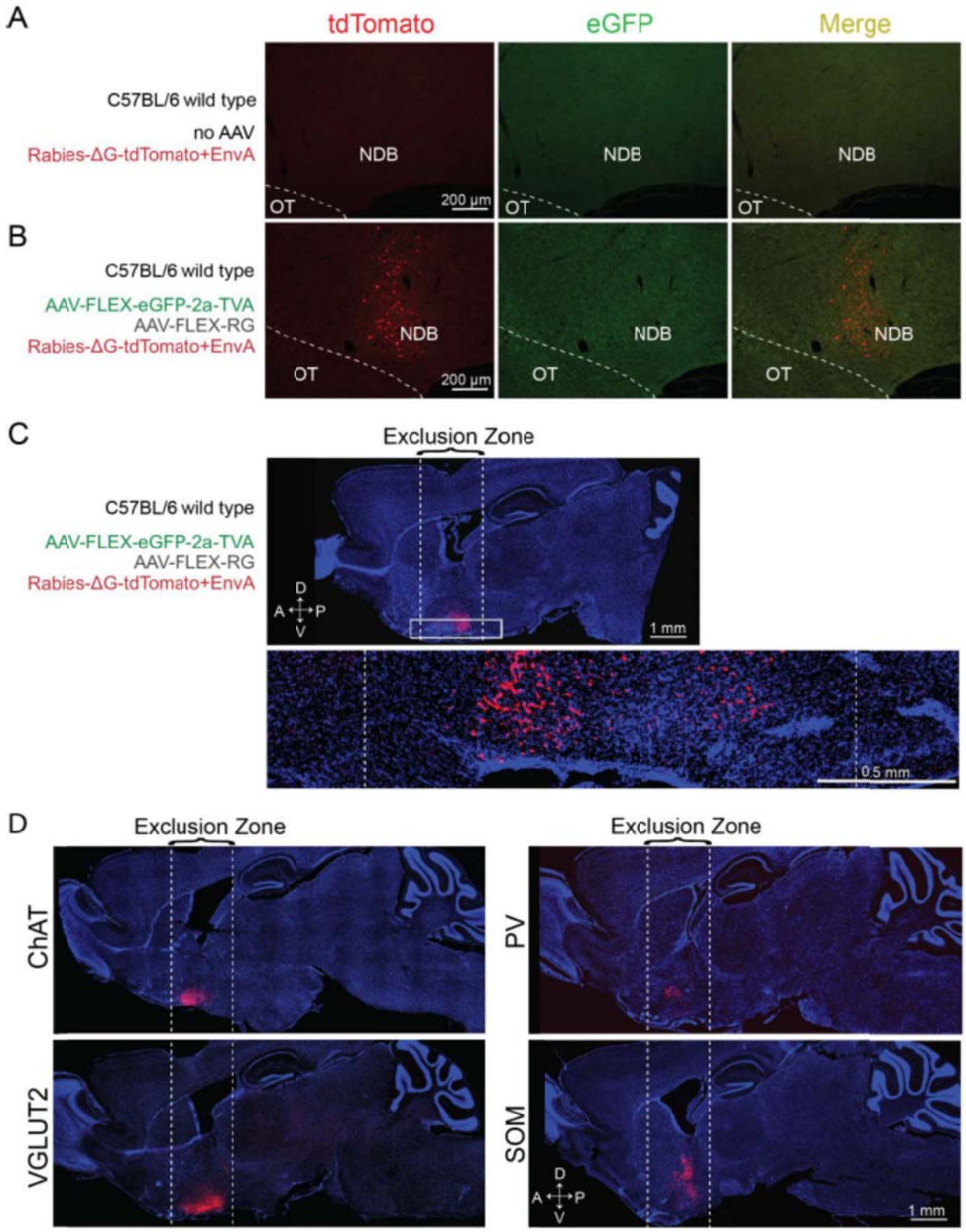

Figure 1 – **figure supplement 2**: **Control experiments for RV tracing of inputs. A)** Injection of RV without prior AAV injection resulted in no tdTomato-labeled neurons, indicating dependence of the RV infection on AAV-induced expression of TVA. **B)** Injection of AAV2-EF1α-FLEX-eGFP-2a-TVA and AAV2-EF1α-FLEX-RG followed by RV injection in the BF of wild-type mice not expressing Cre led to no eGFP expression, indicating Cre-dependence of the AAV vector. However, tdTomato-labeled neurons were observed at the injection site (radius < 500 μm), most likely due to the leaky expression of a low level of TVA, as previously noted(Miyamichi et al., 2013; Wall et al., 2013) **C)** Upper panel, Sagittal view of the experiment shown in B (but a different brain sample), with tdTomato expression near the injection site but not outside of the exclusion zone. Lower panel, enlarged view of the region in the white rectangle. **D)** Sagittal view of brain samples injected with AAV2-EF1α-FLEX-eGFP-2a-TVA followed by RV in the BF of different Cre lines (without AAV2- EF1α-FLEX-RG that enables transsynaptic spread of RV) to determine the spatial extent of the exclusion zone in the RV tracing experiments. After excluding the horizontal limb of the diagonal band of Broca (part of the BF region targeted), we found very few (< 30 per brain) labeled cells beyond 850 μm. Subsequent analyses were thus performed only in coronal sections > 850 μm from the injection site and outside of the horizontal limb of the diagonal band of Broca.

Figure 1 – figure supplement 3.

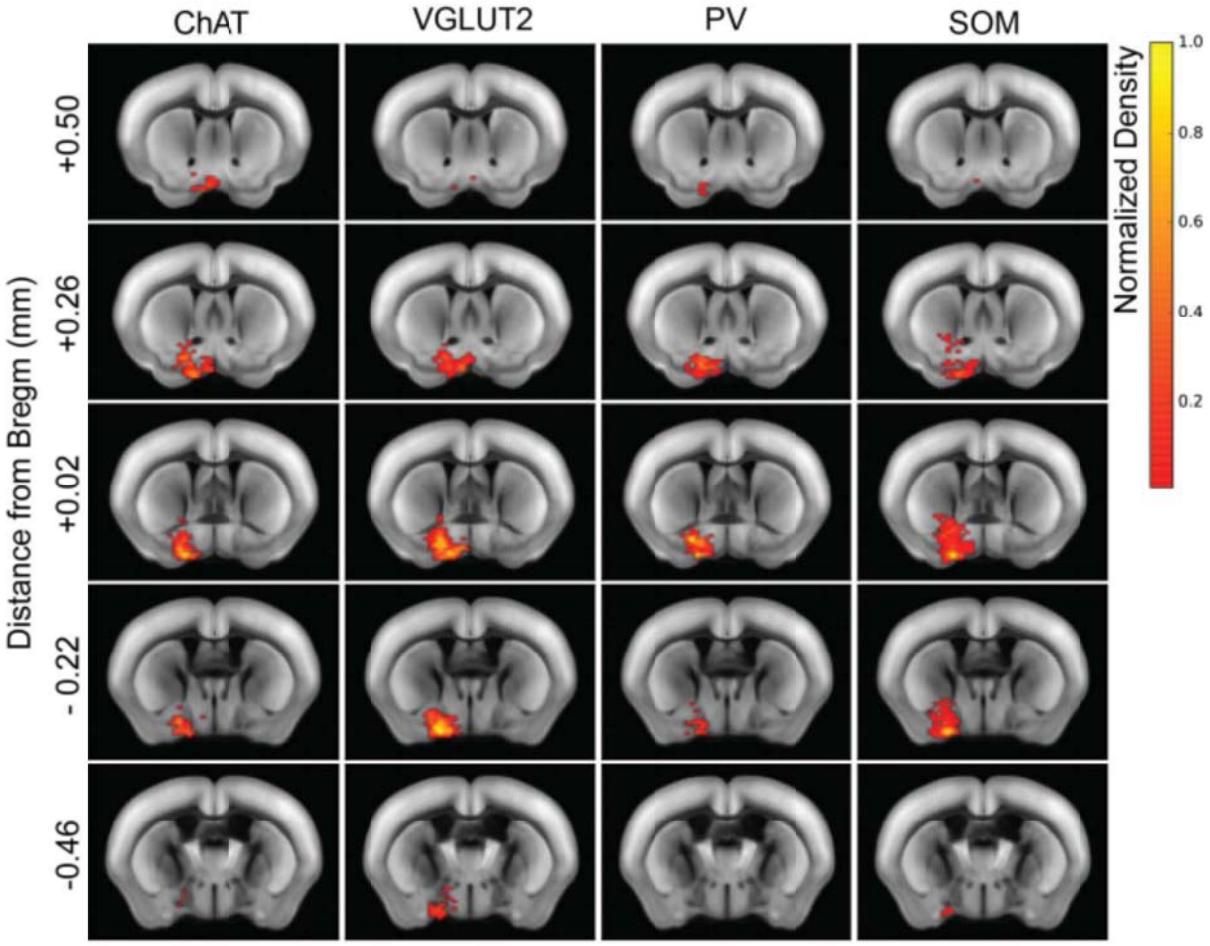

Figure 1 – figure supplement 3: Heat map distribution of starter cells.
Normalized starter cell density across all samples for each cell type. Each brain slice depicts the density accumulated from an anterior-posterior axis range of 0.24 mm.

Figure 1 – figure supplement 4.

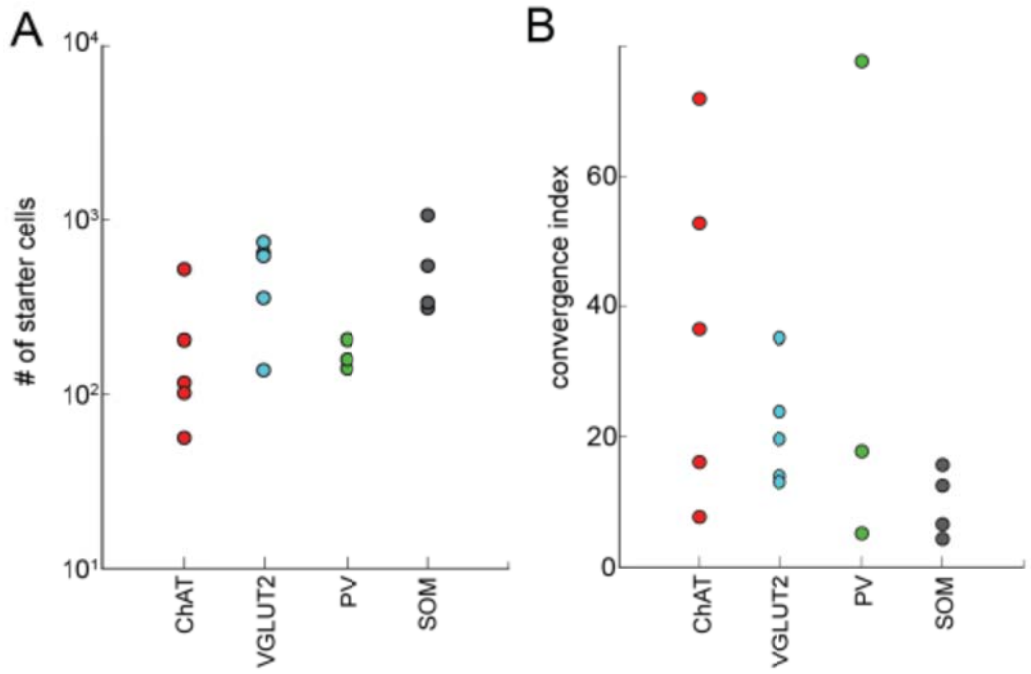

Figure 1 – figure supplement 4: The relationship between the numbers of starter cells and input cells.

A) The total number of starter cells for each brain sample. **B)** The convergence index (input cell count/starter cell count) for each brain sample grouped by cell-type.

Figure 4 – figure supplement 1.

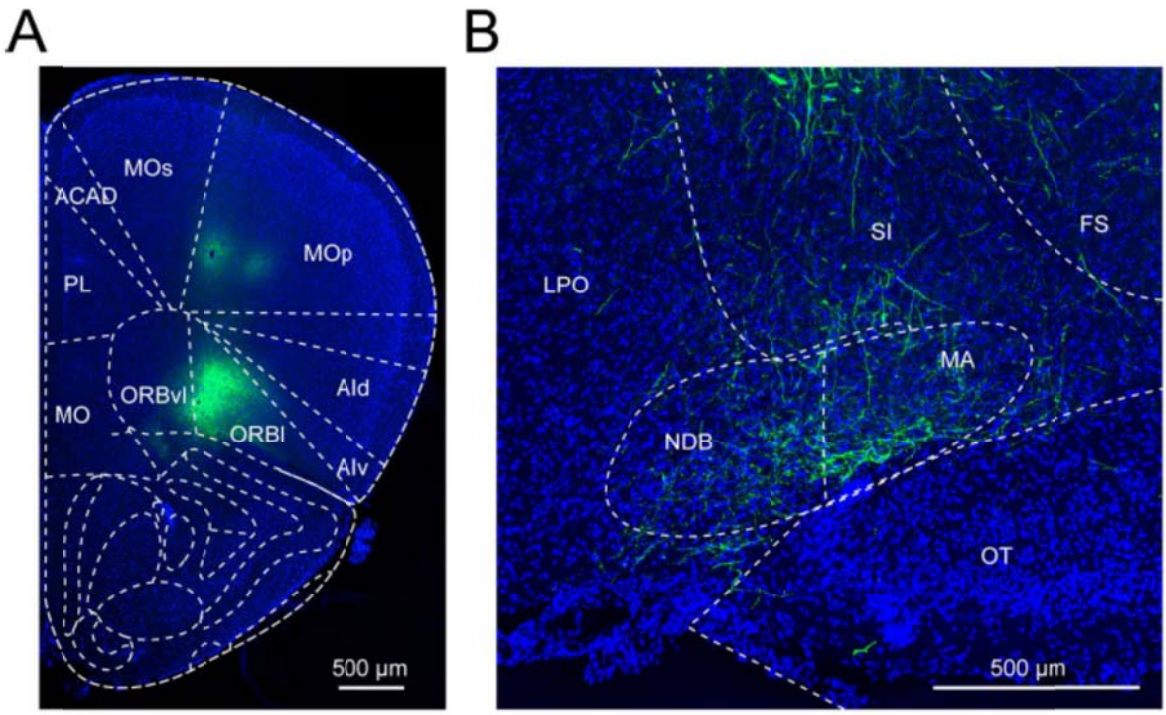

Figure 4 – figure supplement 1: Basal forebrain input from the prefrontal cortex.
A) Example fluorescence image of a coronal section at the virus injection site in the prefrontal cortex (PFC). **B)** Example fluorescence image of the PFC axon fibers in the basal forebrain from the same experiment as shown in panel A.

Figure 7 – **figure supplement 1**:

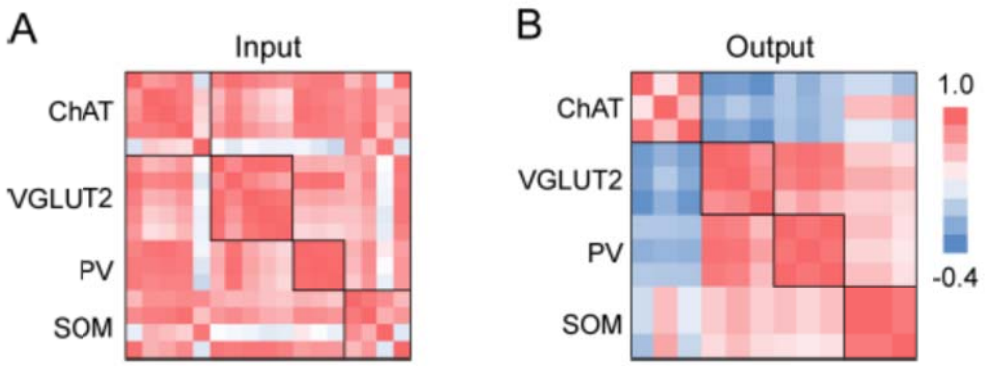

Figure 7 – **figure supplement 1**: **Correlation coefficients between individual brain samples for input and output distributions.**
A) Input. **B)** Output. Note the higher CCs within the boxes along the diagonal (between samples of the same cell type) than those outside of the boxes (between samples of different cell types). The CCs exactly along the diagonal (each brain sample with itself, CC = 1) were excluded from analysis.

CHAPTER 3
Neurotensin Neuronal Circuits for NREM sleep control

Summary

Sleep is a fundamental animal behavior observed widely in the animal kingdom, but the neural circuits generating sleep remain poorly understood. A crucial step in understanding the neural circuits controlling sleep is to identify the sleep-promoting neurons. Most of the well-known sleep-promoting neurons are GABAergic neurons. In this study, we identified neurotensin positive neurons in the Preoptic area (POA), posterior thalamus (pTh), and ventrolateral periaqueductal gray (vlPAG) are NREM sleep-promoting neurons. I examined the reciprocal connections of these three populations, since they have the same sleep regulation function. Besides, I also performed anatomical screening for candidate sleep neurons by detecting the excitatory inputs to these three sleep-promoting neurons. In the Edinger-Westphal nucleus (EW), we also identified cholecystokinin (CCK) and Calcitonin gene-related peptide alpha (Calca) neurons are NREM sleep-promoting neurons. The most interesting thing is that the CCK neurons in the EW (CCK^{EW}), Calca neurons in the EW ($Calca^{EW}$), and NTS neurons in the vlPAG (NTS^{vlPAG}) form reciprocal connections to each other by anatomical analysis.

Introduction

Sleep is an innate behavioral which was controlled by a circadian clock, homeostatic processes, and neuronal circuits. Flip-flop theory proposed by Saper could be used to describe the regulation of sleep-wake circuit mechanism through mutually inhibitory interaction between Sleep-promoting neurons and wake-promoting neurons (Saper et al., 2001). Recently, GABAergic neurons in the VLPO, somatostatin GABAergic neurons in the BF, and GABAergic neurons in the parafacial zone (PZ) are characterized as sleep-promoting neurons (Anaclet et al., 2014; Sherin et al., 1996; Xu et al., 2015). However, these sleep-promoting neurons are spatially intermingled with wake-active neurons. This makes it hard to target the sleep neurons and do the circuit analysis. A crucial step in understanding the sleep neural circuits is to identify a good biomarker to label sleep promoting neurons.

Neurotensin (NTS) is characterized as a neurotransmitter in the central nervous system (Kasckow and Nemeroff, 1991). NTS neurons are located in numerous brain areas, such as basal forebrain, hypothalamus, thalamus, amygdala, ventrolateral periaqueductal gray (vlPAG), and nucleus accumbens (Uhl and Snyder, 1976). NTS has neuromodulatory actions on multiple brain functions including motor, analgesia, hypothermia, and sleep-wake regulation. However, the NTS works on the sleep-wake regulation still has controversial results.

In previous study, EEG recordings were utilized to evaluate the effects of intracerebroventricular administered NTS during sleep-wake cycle. NTS was found to decrease the EEG slow waves activity in the cortex and hippocampus in rats. The results support that NTS increases the arousal level and decreases the sleep time (Castel et al., 1989; Robledo et al., 1995). Besides, activation of Cholinergic BF neurons by NTS microinjection also decreases the NREM sleep, but increases the wakefulness and REM sleep (Cape et al., 2000). However, in the NTS receptor (NTSR) knockout mice study, NTSR knockouts exhibited more wake and less NREM sleep rebound after sleep deprivation (Fitzpatrick et al., 2012). Orexin neurons (wake-promoting neurons) were inhibited by NTS neurons in the lateral hypothalamus by using pharamacogenetic activation method (Goforth et al., 2014). Both of these studies implied that NTS also play an important role to induce NREM sleep.

In this work, we used optogenetics method to activate NTS neurons in the preoptic area (POA), posterior thalamus (pTh), or ventrolateral periaqueductal gray (vlPAG) to examine the effects of NTS neurons on sleep-wake regulation. We also examined the mutual connection of these NTS neurons and their upstream neurons by rabies virus (RV)-mediated trans-synaptic retrograde tracing method. Furthermore, we also identified local NREM sleep circuits in the vlPAG area.

Results

NTS neurons in POA, pTh, and vlPAG are NREM sleep-promoting neurons

Most sleep-active neurons are identified by c-Fos immunostaining followed by sleep rebound after sleep deprivation. It is hard to find or identify a molecular marker to label the specific sleep-promoting neurons. In my lab previous publication, we collected the GABAergic neurons in the POA by retrograde labeling from the TMN (wake promoting area) and sorted the cell with translating ribosome affinity purification (TRAP) (Heiman et al., 2008). Then, we performed the RNA sequencing experiment (RNA-Seq) to reveal multiple genes enriched in this $GABA^{POA\rightarrow TMN}$ neurons relative to the input total RNA (Chung et al., 2017). We identified some neuropeptides have been implicated in sleep regulation, including NTS, corticotropin-releasing hormone (CRH), preprodynorphin (Pdyn) and cholecystokinin (CCK) (Dalal et al., 2013; Goforth et al., 2014; Kimura et al., 2010; Mansbach and Lorenz, 1983). Since NTS has some controversial effects on sleep regulation, I try to measure the sleep function by using optogenetic stimulation in NTS-cre line mouse (Leinninger et al., 2011).

To test the NTS neurons function in sleep regulation, we tagged these neurons with channelrhodopsin-2 (ChR2) by injecting an adeno-associated virus (AAV) vector (AAV-EF1α-DIO-hChR2-eYFP) and implanted an optic fiber into the POA, posterior thalamus (pTh) or vlPAG where NTS neurons form a cluster of NTS-cre mice. In the POA NTS neurons, laser stimulation (10 Hz, 2 min/trial, randomly applied every 5-30 min) caused a strong and immediate increase in NREM sleep at the expense of both wakefulness and REM sleep (Fig 1A). In the pTh, ChR2-mediated activation of NTS neurons caused a strong increase in NREM sleep and decrease in wakefulness and REM sleep (Fig. 1B). Optogenetic activation of NTS neurons in the vlPAG also caused a significant increase in NREM sleep and a complementary decrease in wakefulness and REM sleep (Fig 1C). In control mice expressing EYFP without ChR2, laser stimulation had no effect on sleep behavior (supplementary Fig. 1A, 1B, 1C). These results show that NTS neurons play an important function of induce NREM sleep in POA, pTh and vlPAG.

The network of these three sleep-promoting NTS neuronal populations

Since all of these NTS neuronal populations in the POA, pTh, and vlPAG have similar behavior function as NREM sleep-promoting neurons, I am wondering whether these three neuronal populations form a mutual or hierarchy connection. I applied pseudotyped rabies virus (rabies △G-EGFP+EnvA, RV) to do monosynaptic retrograde tracing (Callaway and Luo, 2015) and followed by fluorescent in situ hybridization (FISH) to detect NTS signal. I injected AAV expressing cre-dependent avian-specific retroviral receptor (TVA) fused with mCherry (AAV2-CAG-DIO-TCB, TCB) and rabies glycoprotein (RG) specifically in each brain region of NTS-cre mice. Two to three weeks later, I injected a RV that only infects NTS cells expressing TVA and requires RG to spread retrogradely to presynaptic cells. After RV infected 1 week, the mouse was sacrificed and the brain tissue was collected to perform FISH experiment. The NTS afferent neurons to the NTS^{POA}, NTS^{pTh}, or NTS^{vlPAG} were list in the table 1. The Figure 2 also the schematic diagram about these 3 neuronal populations. Based on the neuronal anatomical

connection results, the NTS^{POA} and NTS^{vlPAG} form a mutual connection. NTS^{POA} send projection to the NTS^{pTh}. NTS neuronal populations in the pTh and vlPAG have no direct connection.

The common excitatory upstream neurons of these three sleep-promoting NTS neurons

Having confirmed that NTS^{POA}, NTS^{pTh}, and NTS^{vlPAG} function as NREM sleep-promoting neurons, however, these three populations only individually increase around 20% NREM sleep percentage compare to control group. Therefore, it is interesting to identify their common glutamatergic inputs. In principle, I expected the common excitatory input neurons may receive different info and directly activate the downstream sleep-promoting neurons in the rostral part (NTS^{POA}), middle part (NTS^{pTh}), and caudal part (NTS^{vlPAG}) local circuits to promote sleep behavior. RV-mediated retrograde tracing from the NTS^{POA}, NTS^{pTh}, or NTS^{vlPAG} followed by FISH to detect vGlut2 signal as excitatory input. The excitatory afferent neurons to the NTS^{POA}, NTS^{pTh}, or NTS^{vlPAG} were list in the table 2. The results revealed that common excitatory projection to the NTS^{POA}, NTS^{pTh}, and NTS^{vlPAG} are located at PAG and posterior hypothalamus area (PH).

CCK and Calca neurons in the EW area are sleep-promoting neurons

Based on my colleagues experiment, the results showed that there are sleep-active neurons in the Edinger-Westphal nucleus (EW). The EW area is enriched with CCK and Calcitonin gene-related peptide alpha (Calca) neurons. Also, CCK is one of sleep-active neuronal candidate marker in our lab previous publication (Chung et al., 2017). It is worth testing the function of CCK^{EW} and CalcaEW in sleep-wake regulation. We injected a Cre inducible AAV-EF1α-DIO-hChR2-eYFP virus into the EW area in CCK-cre (Taniguchi et al., 2011) line or Calca-cre (Carter et al., 2013) line mouse. Laser stimulation (10 Hz, 2 min/trial, randomly applied every 5-30 min) in freely moving mice, and wake, REM, and NREM sleep were classified based on EEG and EMG recordings. Activation of the CCK^{EW} or $Calca^{EW}$ caused a strong increase in NREM sleep and decreases in both REM sleep and wakefulness (Fig. 3A and 3B). EYFP expression without ChR2 in the EW of Claca-cre line mice, optogenetic stimulation had no change in sleep behavior (supplementary Fig. 2A). The results suggest that CCK^{EW} and $Calca^{EW}$ are sleep-promoting neurons.

The local sleep neuronal circuits in the vlPAG and EW area

We have identified NTS^{vlPAG}, CCK^{EW}, and $Calca^{EW}$ as sleep-promoting neurons. The three neuronal populations are close to each other. Also, they have the same function to induce NREM sleep. I tested whether these three neuronal populations could connect to each other and form a circuit. I took mutant TVA receptor (TC66T) instead of the TCB to prevent local contamination (Miyamichi et al., 2013). I expressed TC66t and RG specifically in each cell type by injecting two Cre-inducible AAV vectors into the vlPAG of NTS-cre, EW of CCK-cre or Calca-cre mice. After 2 to 3 weeks later, the RV was injected into the same position. The mouse brain was collected after 1 week retrograde labelling. I applied FISH experiment followed the trans-synaptic RV labelling. The NTS signal was co-labelled with monosynaptic retrograde cells in the

vlPAG in the CCK^{EW} retrograde tracing mouse (Fig. 4A) and the $Calca^{EW}$ retrograde tracing mouse (Fig. 5A). The results indicate that NTS^{vlPAG} directely project to the CCK^{EW} and $Calca^{EW}$. The CCK signal was also detected in the retrograde labelled neurons in the EW in the NTS^{vlPAG} retrograde tracing experiment (Fig. 4B) and the $Calca^{EW}$ retrograde tracing experiment (Fig. 6A). The upstream labelled neurons of the NTS^{vlPAG} and CCK^{EW} were also co-labelled with Calca in the EW (Fig. 5B and 6B). All of these results explain that NTS^{vlPAG}, $Calca^{EW}$ and CCK^{EW} formed a mutual connection in the PAG and EW area.

Discussion and future direction

Due to the technical innovations in the past few years, we can detect more detail of the neuronal function in the specific cell type and brain region. In this study, we found that NTS neurons in the POA, pTh, and vlPAG are sleep-promoting neurons by optogenetic manipulation, although in previous research demonstrated that intracerebroventricular administered NTS or directly injected NTS into BF caused wakefulness (Castel et al., 1989; Robledo et al., 1995). The results imply that NTS might not be a sleep factor and not all NTS neurons in the brain are sleep-promoting neurons. Identification of these three new sleep-promoting neuronal populations also will help us to dissect the sleep circuits.

I applied RV retrograde tracing method and FISH experiment to test whether NTS^{POA}, NTS^{pTh}, and NTS^{vlPAG} form a connection since they have the same NREM sleep-promoting function. I originally expected that there are hierarchical connections of these three NTS neuronal populations, because of the NTS^{POA} are GABAergic neurons and the other two populations are Glutamatergic neurons. I assumed that NTS^{POA} might be the lowest level of these three populations. However, the results showed that NTS^{POA} still send projections to the NTS^{pTh} and NTS^{vlPAG}. I explained that these three neuronal populations can functionally promote the NREM sleep behavior. However, they might not directly communicate to each other in the sleep-wake regulation function. Thus, these three neuronal populations might separately promote the NREM sleep and locally do their functional regulation.

The excitatory inputs to the NTS^{POA}, NTS^{pTh}, and NTS^{vlPAG} provide us a hint to test whether these excitatory neurons are sleep-promoting neurons or not. If there has a common excitatory input to these three neuronal populations, it might be a big sleep-promoting center. I identified common excitatory neurons in the PAG and PH, although it is sparse. There are no obvious common neuronal clusters send excitatory projection to the NTS^{POA}, NTS^{pTh}, and NTS^{vlPAG}. PAG is a big region of the brain and does responsibility to many different functions. It has been purposed that the PAG is involved in vocalization, micturition, and thermoregulation, and contributes to mechanisms of arousal and control of REM sleep (Benarroch, 2012). The activity of neurons in the PH is thought to contribute to the production of wakefulness and electroencephalograph desynchronization (Szymusiak and McGinty, 2008) . There has a report showed that GABA release in the PH mediates inhibition of posterior hypothalamic neurons would facilitate NREM sleep (Nitz and Siegel, 1996). According to all of these results, if there has glutamatergic sleep-promoting neurons in the PAG and PH area, the neurons might be intermingled with other wake-active neurons. It still needs more experiments to verify the function of these excitatory neurons found in the PAG and PH. In the future, I might be able to apply the retrograde tracing co-expression with ChR2 to label the excitatory neurons and verify the function by optogenetic manipulation.

In the vlPAG and the EW, we found that NTS^{vlPAG}, $Calca^{EW}$ and CCK^{EW} are all NREM sleep-promoting neurons. The anatomical tracing results also showed these three neuronal populations can form reciprocal connections. It implies that these 3 populations form local

circuits and may reinforce each other to produce and maintain the NREM sleep. In the future, I will express ChR2 in the NTS^{vlPAG}. Then, I measure the sleep effect by downstream fiber stimulation in the EW and vice versa. This experiment can test whether the local circuit form by these 3 neuronal populations performs the same function together or separately.

Materials and Methods

Animals

All experimental procedures were approved by the Animal Care and Use Committee at the University of California, Berkeley. NTS-IRES-Cre (Jackson stock numbers 017525) and CCK-IRES-Cre mice (Jackson stock numbers 012706) were obtained from Jackson Laboratory. Calca-IRES-Cre mice were obtained from Richard Palmiter. Pdyn-IRES-Cre mice were obtained from Bradford Lowell. Animals were housed on a 12-h dark/12-h light cycle (light on between 7:00 and off at 19:00) with free access to food and water. Mice with implants for EEG/EMG recordings, optogenetic stimulation were housed individually. Mice injected with viruses for trans-synaptic tracing were housed in groups of up to 5 animals.

Surgical Procedures

Adult (10- to 20-week-old) mice were anaesthetized with isoflurane (5% induction, 1.5% maintenance) and placed on a stereotaxic frame. Body temperature was kept stable throughout the procedure by using a heating pad. A craniotomy (1 mm diameter) was made for virus injection and optical fiber implantation. The stereotaxic coordinates were as follows. POA: anteroposterior (AP) 0 mm, mediolateral (ML) 0.7 mm, dorsoventral (DV) 5.2 mm; pTh: AP -3.4 mm, ML 1.8 mm, DV 3.0- 3.1 mm; EW: AP 4 mm, ML 0 mm, DV 3.2- 3.3 mm; vlPAG: AP -5.0 mm, ML 0.6 mm, DV 3.3mm.

For EEG/EMG recording experiment, a EEG reference screw was inserted into the skull on top of the left cerebellum. EEG recordings were made from two screws. The screws were bilaterally inserted into the skull 2.5 mm from the midline and 3.0 mm posterior to the bregma. One EMG electrode was inserted into the neck musculature. Insulated leads from the EEG and EMG electrodes were soldered to a pin header, which was secured to the skull using dental cement.

For optogenetic manipulation experiments, AAV2-EF1α-DIO-ChR2–eYFP or AAV2-EF1α-DIO–eYFP (produced by University of North Carolina Vector Core) virus was loaded into a sharp micropipette mounted on a Nanoject II attached to a micromanipulator and slowly injected into the target area (total 300 nl). We then implanted optic fibers into the target region. Dental cement was applied to completely cover the exposed skull. After surgery, mice were allowed to recovery for at least 2-3 weeks before experiments.

Optogenetic Manipulations and Polysomnographic recordings

For optogenetic stimulation experiments, fiber optic cable (200 μm diameter; ThorLabs) was attached through an FC/PC adaptors to a 473 nm blue laser diode (Shanghai Laser & Optics Century Co. Ltd.). During experiments, each trial was applied with 10 Hz pulse train (6 mW laser power at fiber tip) lasting for 120 sec. The inter-trial interval was chosen randomly between 5 to 30 minutes. EEG and EMG electrodes were connected to flexible recording cables via a mini-connector. The signals were recorded and amplified using TDT RZ5 amplifier (bandpass filter, 1–750 Hz; sampling rate, 1,500 Hz). EEG and EMG signals were referenced to a common ground

screw, place on top of the cerebellum. The EEG signal was calculated by the difference between the voltage potentials recorded from the EEG electrode and the reference electrode. The EMG signal was calculated by the difference between the potentials from the EMG electrode and reference electrode. Spectral analysis was performed using fast Fourier transform (FFT). NREM, REM and wake states were semi-automatically classified using custom-written MATLAB software. (wakefulness: desynchronized EEG and high EMG activity; NREM sleep: synchronized EEG with high power at 0.5–4 Hz and low EMG activity; REM sleep: desynchronized EEG with high power at theta frequencies (6–9 Hz) and low EMG activity)

Rabies Virus Tracing

For local retrograde tracing, AAV-CAG-FLExloxP-TC66T (2.3×10^{12} gc/mL) and AAV2-CAG-FLExloxP-RG (3.5×10^{12} gc/mL) was mixed at a 1:1 ratio and stereotaxically injected into specific brain region. For long range retrograde tracing, AAV-CAG-FLExloxP-TC66T was change to AAV-CAG-FLExloxP-TCB (3.0×10^{12} gc/mL). Two weeks later, EnvA-pseudotyped, glycoprotein-deleted, and GFP-expressing rabies virus (RV) were injected into the same position. Mice were euthanized 1 week later and start to do tissue processing.

Tissue Processing

Mice were deeply anesthetized with isoflurane and transcardially perfused with 20 ml of phosphate-buffered saline (PBS) (pH 7.2) followed by 20 ml of 4% paraformaldehyde (PFA) in PBS. Brain tissue was carefully removed, post-fixed in 4% PFA in PBS at 4 °C for 36 hr, dehydrated in 30% sucrose in PBS for 48 hr, and embedded in Tissue Freezing Medium (Triangle Biomedical Sciences, Cincinnati, OH, Waltham, MA). Brains were cut in 20 μm coronal sections using a cryostat (Thermo Scientific).

Fluorescence In Situ Hybridization (FISH)

FISH was done by using an RNAscope assay kit according to the manufacturer's instructions (RNAscope® Fluorescent Multiplex Reagent Kit, Cat # 320850, Advanced cell Diagnostics). Briefly, brain samples were treated with 2% H_2O_2 in PBS for 10 min. Then, put into retrieval buffer with high temperature (95~100°C) for 5 min. Protease treatment for 30 min at 40°C. After washing, specific RNA probe was added into sample to do hybridization for 2 hr at 40°C. To develope the fluorescence signal by adding fluorescence buffer 1, 2, 3 and 4 in order with indicated time period. Fluorescence images were taken using a fluorescence microscope (BZ-X700, Keyence) or slide scanner (Nanozoomer-2.0RS, Hamamatsu).
All probes were bought from Advanced cell Diagnostics. Calca probe (Mm-Calca, 417961); CCK probe (Mm-CCK, 402271); eGFP probe (EGFP-C3, 400281-C3); NTS probe (Mm-Nts, 420441); vGlut2 (Mm-Slc17a6, 319171)

Figures and Tables

Figure 1.

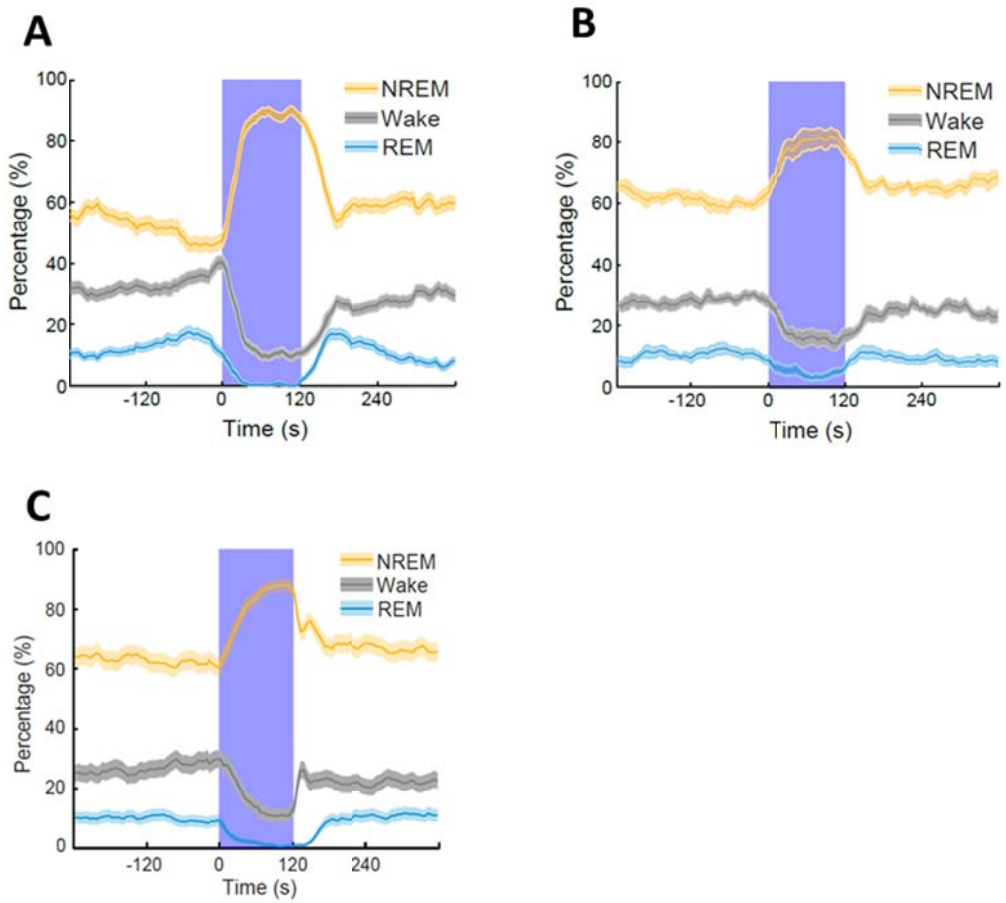

Figure 1. Optogenetic activation of NTS neurons enhances NREM sleep.
(A) activation site in POA, (B) activation site in pTh, (C) activation site in vlPAG. Percentage of time in NREM, REM, or wake state before, during, and after laser stimulation. Blue shading, laser stimulation (10 Hz, 120 s).

Figure 2.

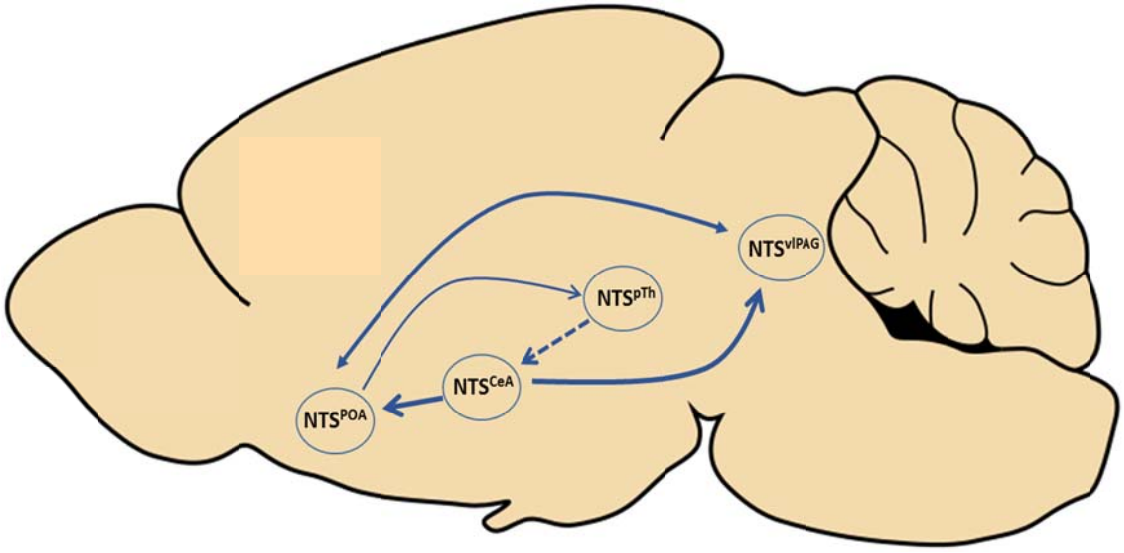

Figure 2. The schematic diagram of NTS neuronal connection in POA, vlPAG, pTh and central amygdala (CeA)

Figure 3.

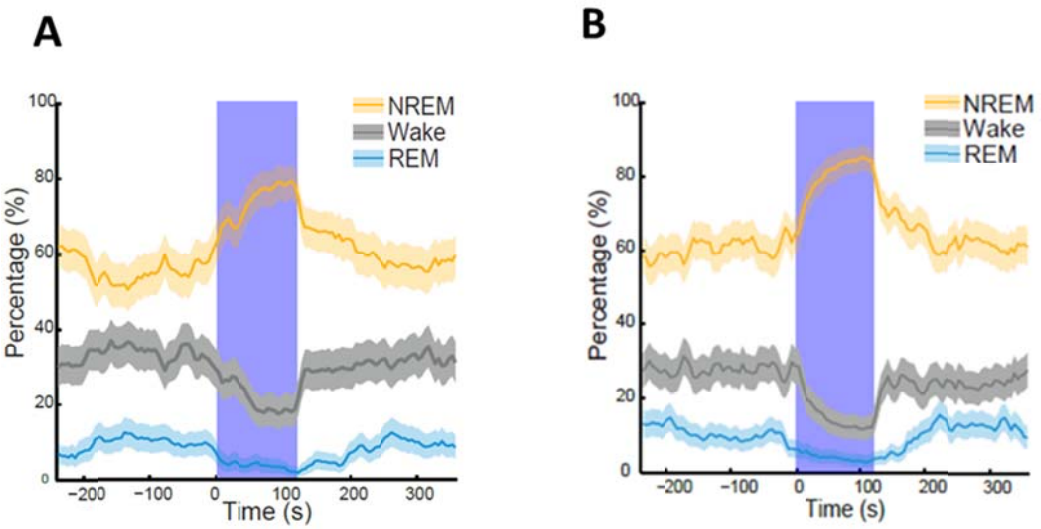

Figure 3. Optogenetic activation experiments of (A) CCK positive neurons (B) Calca positive neurons in EW region enhances NREM sleep. Percentage of time in NREM, REM, or wake state before, during, and after laser stimulation. Blue shading, laser stimulation (10 Hz, 120 s).

Figure 4.

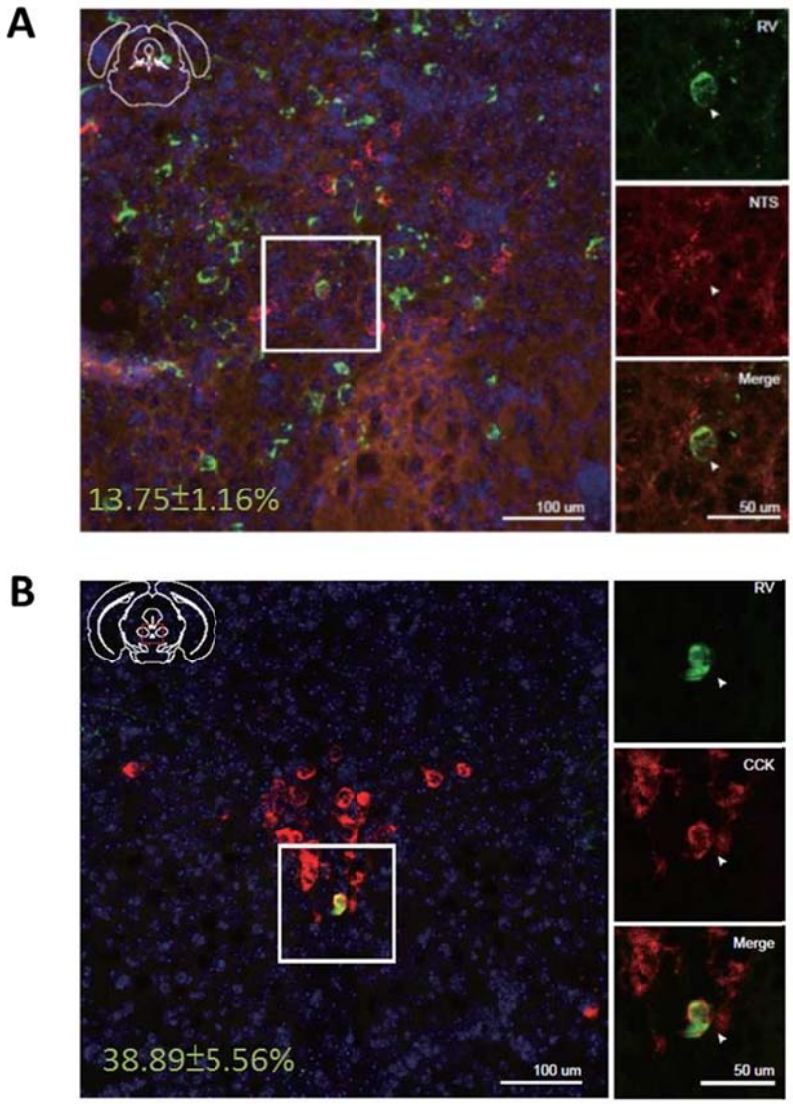

Figure 4. The reciprocal connection between NTS ^{vlPAG} and CCK^{EW}
(A) Left, fluorescence image of vlPAG in a CCK-Cre mouse. NTS and RV double-positive cells as a percentage of the total RV positive cells in the vlPAG are indicated. The data are presented as the means± s.e.m. of three mice. Right, images enlarged view of the region in white box . Arrowhead: indicate the cell express NTS and labeled with RV. **(B)** Left, fluorescence image of EW in a NTS-Cre mouse. CCK and RV double-positive cells as a percentage of the total RV positive cells in the EW are indicated. The data are presented as the means± s.e.m. of three mice. Right, images enlarged view of the region in white box . Arrowhead: indicate the cell express CCK and labeled with RV.

Figure 5.

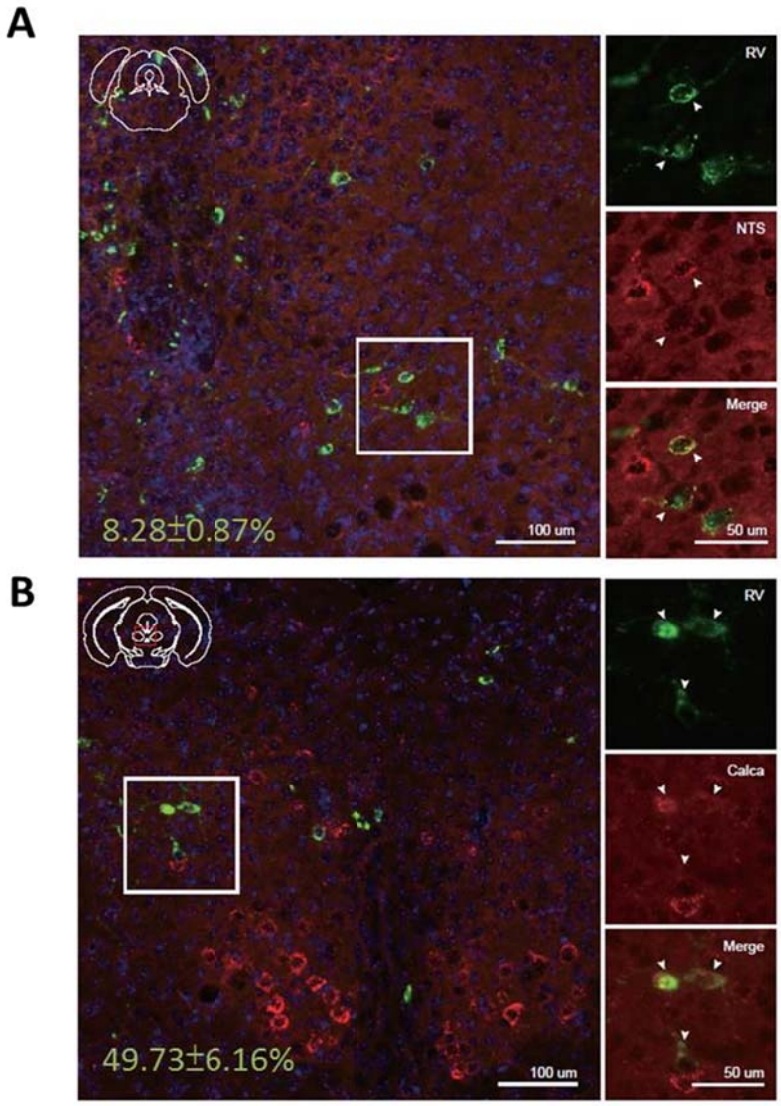

Figure 5. The reciprocal connection between NTS ^{vlPAG} and Calca^{EW}
(A) Left, fluorescence image of vlPAG in a Calca-Cre mouse. NTS and RV double-positive cells as a percentage of the total RV positive cells in the vlPAG are indicated. The data are presented as the means± s.e.m. of three mice. Right, images enlarged view of the region in white box . Arrowhead: indicate the cell express NTS and labeled with RV. **(B)** Left, fluorescence image of EW in a NTS-Cre mouse. Calca and RV double-positive cells as a percentage of the total RV positive cells in the EW are indicated. The data are presented as the means± s.e.m. of three mice. Right, images enlarged view of the region in white box . Arrowhead: indicate the cell express Calca and labeled with RV.

Figure 6.

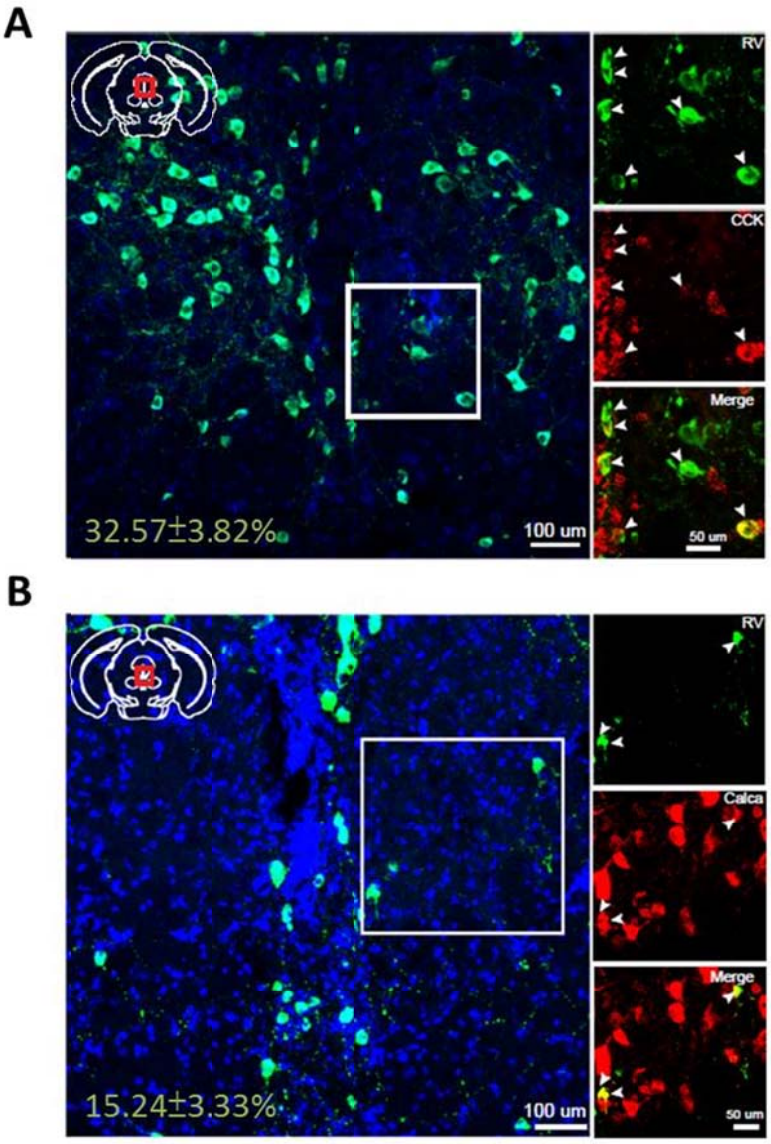

Figure 6. The reciprocal connection between CCK^{EW} and Calca^{EW}
(A) Left, fluorescence image of EW in a Calca-Cre mouse. CCK and RV double-positive cells as a percentage of the total RV positive cells in the EW are indicated. The data are presented as the means± s.e.m. of three mice. Right, images enlarged view of the region in white box . Arrowhead: indicate the cell express CCK and labeled with RV. **(B)** Left, fluorescence image of EW in a CCK-Cre mouse. Calca and RV double-positive cells as a percentage of the total RV positive cells in the EW are indicated. The data are presented as the means± s.e.m. of three mice. Right, images enlarged view of the region in white box . Arrowhead: indicate the cell express Calca and labeled with RV.

Table 1.

NTS Starter cell location	Afferent NTS neuron
Preoptic area (POA)	TU (Tuberal nucleus), Lateral hypothalamus (LH), PSTN (Parasubthalamic nucleus), Central amygdalar nucleus (CEA), Medial amygdalar nucleus (MEA), Med mammillary nu (MM), Substamtia nigra compact (SNC), **ventrolateral periaqueductal gray (vlPAG),** parabrachial nucleus (PB), Medial vestibular nucleus (MV)
ventrolateral periaqueductal gray (vlPAG)	**Lat preoptic area (LPO),** **Medial preoptic area (MPO)**, Central amygdala (CEA), Subthalamic nu (STh)
posterior thalamus (pTh)	**Medial preoptic area (MPO)**, External cx inferior colliculus (ECIC), Spinal vestibular nu (SpVe)

Table 1. Whole-brain NTS input neurons to the three specific NTS neuron clusters in POA, vlPAG, and pTh. The indicated afferent NTS neurons are repeated appearance in 3 mice.

Table 2.

NTS Starter cell location	Afferent vGlut2 positive neurons	
Preoptic area (POA)	Lat hypothalamus (PLH), Posterior hypothalamus (PH), dorsomedial hypothalamic nucleus (DMH), ventromedial hypothalamic nucleus (VMH), Medial habenula (MH), Medial amygdalar nucleus (MEA), Mesencephalic retic form (mRt),	Med mammillary nu (MM), Vent tegmental area (VTA), Red nucleus, periaqueductal gray (PAG), Interpedunc nu (IPR), Parabrachial nu (PB), Med vestib nu (MV),
ventrolateral periaqueductal gray (vlPAG)	Medial preoptic area (MPA), Ventral pallium (VP) , Peduncular part lat hy (PLH), Mediodorsal thalamic nu (MD), Paraventric hypothalamus (PaD), Supraoptic nucleus (SO), Paravent hy (PaL), Stria medullaris thal (SM), VMH, DMH, Subincertal nu (Sub), Lateral habenula (LHb), Lateral hypothalamus (LH), posterior hypothalamus (Ph),	Parasubthalamic nu (PSTh), Precommissural nu (PrC), Reticular formation , PAG, lPAG, Anterior pretectal nu (APT), Intermed gray area (InG), Central nu inf colliculus (CIC), Dorsomed tegmental area (DMTg), Intermed reticular nu (IRt), Med vestib nu (MV), vestibulocerebellar nucleus (VeCb), Gigantocellular reticular nu (Gi), Parvicell reticular nu (PCRT), Spinal trigeml nu (SP5O)
posterior thalamus (pTh)	Paraventricular thal nu (PVA), Medial preoptic nu (MPO), Dorsalme hypothalamus (DMH), LP thal nu (LPMR), Posterior hypothalamus (PH), Ant pretectal nu (APTD), Post thal nuclear group (Po), LP thal nu (LPMC), External cx inferior colliculus (ECIC), Superior colliculus (Ing/Dpg),	PAG, Dorsal nu lateral lemniscus (DLL), Principle sensory trigem nu (Pr5), Parabrachial nu (PB), Intermed reticular nu (IRt), Pontine reticular nu (PnC), Dentate nu (Dn), Gigantocellular reticular nu (Gi), superior vestibu nu (SuVe), Fastigial nucleus (FN), Med longitudinal fasciculus (mlf)

Table 2. Whole-brain glutamatergic input neurons to the three specific NTS neuron clusters in POA, vlPAG, and pTh. The indicated afferent vGlut2 neurons are repeated appearance in 3 mice.

Supplemental Figures

Supplemental Figures 1

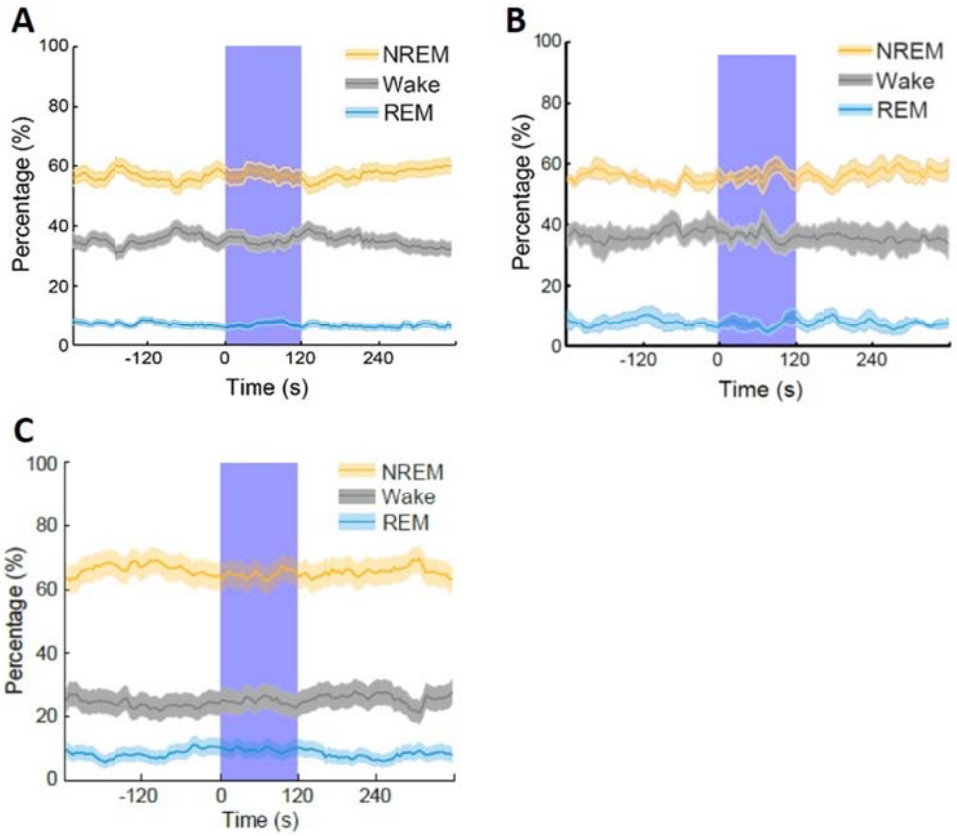

Supplementary Figure 1. Optogenetic activation of NTS neurons tagged with EYFP as control. (A) activation site in POA, (B) activation site in pTh, (C) activation site in vlPAG. Percentage of time in NREM, REM, or wake state before, during, and after laser stimulation. Blue shading, laser stimulation (10 Hz, 120 s).

Supplemental Figures 2

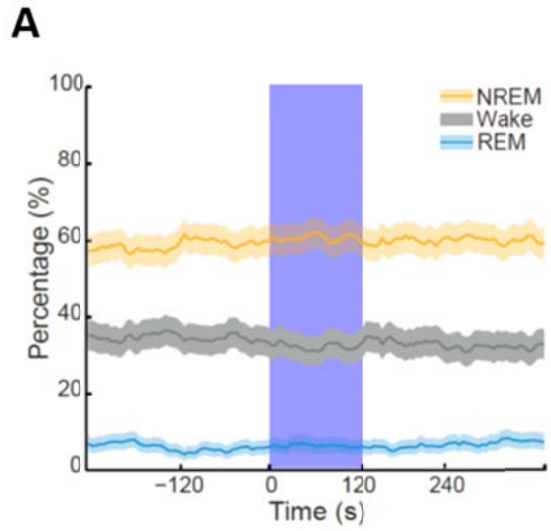

Supplementary Figure 2. Optogenetic activation of Calca neurons tagged with EYFP as control. (A) activation site in EW. Percentage of time in NREM, REM, or wake state before, during, and after laser stimulation. Blue shading, laser stimulation (10 Hz, 120 s).

Supplemental Table 1

	NTS^{vlPAG}--> CCK^{EW}			CCK^{EW}-->NTS^{vlPAG}		
	NTS+ & RV+ cell number	total RV+ cells	percentage (%)	CCK+ & RV+ cell number	total RV+ cells	percentage (%)
Mouse 1	4	27	14.81	1	2	50.00
Mouse 2	4	35	11.43	1	3	33.33
Mouse 3	3	20	15.00	1	3	33.33
Mean±s.e.m.			13.75±1.16			38.89±5.56
	NTS^{vlPAG}--> $Calca^{EW}$			$Calca^{EW}$--> NTS^{vlPAG}		
	NTS+ & RV+ cell number	total RV+ cells	percentage (%)	Calca+ & RV+ cell number	total RV+ cells	percentage (%)
Mouse 1	1	10	10.00	6	11	54.55
Mouse 2	1	14	7.14	4	7	57.14
Mouse 3	1	13	7.69	3	8	37.50
Mean±s.e.m.			8.28±0.87			49.73±6.16
	CCK^{EW}--> $Calca^{EW}$			$Calca^{EW}$--> CCK^{EW}		
	CCK+ & RV+ cell number	total RV+ cells	percentage (%)	Calca+ & RV+ cell number	total RV+ cells	percentage (%)
Mouse 1	6	15	40.00	3	14	21.43
Mouse 2	7	23	30.43	2	20	10.00
Mouse 3	6	22	27.27	3	21	14.29
Mean±s.e.m.			32.57±3.82			15.24±3.33

Supplementary Table 1. The actual cell counts of the reciprocal connection between indicated cell types and regions

References

Allada, R., White, N.E., So, W.V., Hall, J.C., and Rosbash, M. (1998). A mutant Drosophila homolog of mammalian Clock disrupts circadian rhythms and transcription of period and timeless. Cell *93*, 791-804.

Anaclet, C., Ferrari, L., Arrigoni, E., Bass, C.E., Saper, C.B., Lu, J., and Fuller, P.M. (2014). The GABAergic parafacial zone is a medullary slow wave sleep-promoting center. Nature neuroscience *17*, 1217-1224.

Asanuma, C. (1989). Axonal arborizations of a magnocellular basal nucleus input and their relation to the neurons in the thalamic reticular nucleus of rats. Proceedings of the National Academy of Sciences *86*, 4746.

Avila, I., and Lin, S.-C. (2014). Distinct neuronal populations in the basal forebrain encode motivational salience and movement. Frontiers in Behavioral Neuroscience *8*.

Bakin, J.S., and Weinberger, N.M. (1996). Induction of a physiological memory in the cerebral cortex by stimulation of the nucleus basalis. Proceedings of the National Academy of Sciences *93*, 11219.

Beier, K.T., Steinberg, E.E., DeLoach, K.E., Xie, S., Miyamichi, K., Schwarz, L., Gao, X.J., Kremer, E.J., Malenka, R.C., and Luo, L. (2015). Circuit Architecture of VTA Dopamine Neurons Revealed by Systematic Input-Output Mapping. Cell *162*, 622-634.

Benarroch, E.E. (2012). Periaqueductal gray: an interface for behavioral control. Neurology *78*, 210-217.

Brown, R.E., Basheer, R., McKenna, J.T., Strecker, R.E., and McCarley, R.W. (2012). Control of Sleep and Wakefulness. Physiological Reviews *92*, 1087-1187.

Bunger, M.K., Wilsbacher, L.D., Moran, S.M., Clendenin, C., Radcliffe, L.A., Hogenesch, J.B., Simon, M.C., Takahashi, J.S., and Bradfield, C.A. (2000). Mop3 is an essential component of the master circadian pacemaker in mammals. Cell *103*, 1009-1017.

Callaway, E.M., and Luo, L. (2015). Monosynaptic Circuit Tracing with Glycoprotein-Deleted Rabies Viruses. The Journal of neuroscience : the official journal of the Society for Neuroscience *35*, 8979-8985.

Cape, E.G., Manns, I.D., Alonso, A., Beaudet, A., and Jones, B.E. (2000). Neurotensin-induced bursting of cholinergic basal forebrain neurons promotes gamma and theta cortical activity together with waking and paradoxical sleep. The Journal of neuroscience : the official journal of the Society for Neuroscience *20*, 8452-8461.

Carter, M.E., Soden, M.E., Zweifel, L.S., and Palmiter, R.D. (2013). Genetic identification of a neural circuit that suppresses appetite. Nature *503*, 111-114.

Castel, M.N., Stutzmann, J.M., Lucas, M., Lafforgue, J., and Blanchard, J.C. (1989). Effects of ICV administration of neurotensin and analogs on EEG in rats. Peptides *10*, 95-101.

Chou, T.C., Bjorkum, A.A., Gaus, S.E., Lu, J., Scammell, T.E., and Saper, C.B. (2002). Afferents to the ventrolateral preoptic nucleus. The Journal of neuroscience : the official journal of the Society for Neuroscience *22*, 977-990.

Chou, T.C., Scammell, T.E., Gooley, J.J., Gaus, S.E., Saper, C.B., and Lu, J. (2003). Critical role of dorsomedial hypothalamic nucleus in a wide range of behavioral circadian rhythms. The Journal of neuroscience : the official journal of the Society for Neuroscience *23*, 10691-10702.

Chung, S., Weber, F., Zhong, P., Tan, C.L., Nguyen, T.N., Beier, K.T., Hormann, N., Chang, W.C., Zhang, Z., Do, J.P*., et al.* (2017). Identification of preoptic sleep neurons using retrograde labelling and gene profiling. Nature *545*, 477-481.
Conner, J.M., Culberson, A., Packowski, C., Chiba, A.A., and Tuszynski, M.H. (2003). Lesions of the Basal Forebrain Cholinergic System Impair Task Acquisition and Abolish Cortical Plasticity Associated with Motor Skill Learning. Neuron *38*, 819-829.
Cullinan, W.E., and Zaborszky, L. (1991). Organization of ascending hypothalamic projections to the rostral forebrain with special reference to the innervation of cholinergic projection neurons. The Journal of comparative neurology *306*, 631-667.
Daan, S., Beersma, D.G., and Borbely, A.A. (1984). Timing of human sleep: recovery process gated by a circadian pacemaker. The American journal of physiology *246*, R161-183.
Dalal, J., Roh, J.H., Maloney, S.E., Akuffo, A., Shah, S., Yuan, H., Wamsley, B., Jones, W.B., de Guzman Strong, C., Gray, P.A*., et al.* (2013). Translational profiling of hypocretin neurons identifies candidate molecules for sleep regulation. Genes & development *27*, 565-578.
DeNardo, L.A., Berns, D.S., DeLoach, K., and Luo, L. (2015). Connectivity of mouse somatosensory and prefrontal cortex examined with trans-synaptic tracing. Nature neuroscience *18*, 1687-1697.
Eggermann, E., Serafin, M., Bayer, L., Machard, D., Saint-Mleux, B., Jones, B.E., and Muhlethaler, M. (2001). Orexins/hypocretins excite basal forebrain cholinergic neurones. Neuroscience *108*, 177-181.
Everitt, B.J., and Robbins, T.W. (1997). CENTRAL CHOLINERGIC SYSTEMS AND COGNITION. Annual Review of Psychology *48*, 649-684.
Fitzpatrick, K., Winrow, C.J., Gotter, A.L., Millstein, J., Arbuzova, J., Brunner, J., Kasarskis, A., Vitaterna, M.H., Renger, J.J., and Turek, F.W. (2012). Altered sleep and affect in the neurotensin receptor 1 knockout mouse. Sleep *35*, 949-956.
Fogle, K.J., Parson, K.G., Dahm, N.A., and Holmes, T.C. (2011). CRYPTOCHROME is a blue-light sensor that regulates neuronal firing rate. Science (New York, NY) *331*, 1409-1413.
Freund, T.F., and Meskenaite, V. (1992). gamma-Aminobutyric acid-containing basal forebrain neurons innervate inhibitory interneurons in the neocortex. Proceedings of the National Academy of Sciences *89*, 738.
Froemke, R.C., Carcea, I., Barker, A.J., Yuan, K., Seybold, B.A., Martins, A.R., Zaika, N., Bernstein, H., Wachs, M., Levis, P.A*., et al.* (2013). Long-term modification of cortical synapses improves sensory perception. Nature neuroscience *16*, 79-88.
Goforth, P.B., Leinninger, G.M., Patterson, C.M., Satin, L.S., and Myers, M.G., Jr. (2014). Leptin acts via lateral hypothalamic area neurotensin neurons to inhibit orexin neurons by multiple GABA-independent mechanisms. The Journal of neuroscience : the official journal of the Society for Neuroscience *34*, 11405-11415.
Grove, E.A. (1988a). Efferent connections of the substantia innominata in the rat. Journal of Comparative Neurology *277*, 347-364.
Grove, E.A. (1988b). Neural associations of the substantia innominata in the rat: Afferent connections. Journal of Comparative Neurology *277*, 315-346.
Haas, L. (2003). Hans Berger (1873–1941), Richard Caton (1842–1926), and electroencephalography. Journal of Neurology, Neurosurgery, and Psychiatry *74*, 9-9.
Hallanger, A.E., Levey, A.I., Lee, H.J., Rye, D.B., and Wainer, B.H. (1987). The origins of cholinergic

and other subcortical afferents to the thalamus in the rat. The Journal of comparative neurology *262*, 105-124.
Hangya, B., Ranade, S.P., Lorenc, M., and Kepecs, A. (2015). Central cholinergic neurons are rapidly recruited by reinforcement feedback. Cell *162*, 1155-1168.
Hara, J., Beuckmann, C.T., Nambu, T., Willie, J.T., Chemelli, R.M., Sinton, C.M., Sugiyama, F., Yagami, K., Goto, K., Yanagisawa, M.*, et al.* (2001). Genetic ablation of orexin neurons in mice results in narcolepsy, hypophagia, and obesity. Neuron *30*, 345-354.
Hassani, O.K., Lee, M.G., Henny, P., and Jones, B.E. (2009). Discharge profiles of identified GABAergic in comparison to cholinergic and putative glutamatergic basal forebrain neurons across the sleep-wake cycle. The Journal of neuroscience : the official journal of the Society for Neuroscience *29*, 11828-11840.
Hasselmo, M.E., and Sarter, M. (2010). Modes and Models of Forebrain Cholinergic Neuromodulation of Cognition. Neuropsychopharmacology *36*, 52.
Heiman, M., Schaefer, A., Gong, S., Peterson, J.D., Day, M., Ramsey, K.E., Suarez-Farinas, M., Schwarz, C., Stephan, D.A., Surmeier, D.J.*, et al.* (2008). A translational profiling approach for the molecular characterization of CNS cell types. Cell *135*, 738-748.
Henny, P., and Jones, B.E. (2006). Vesicular glutamate (VGlut), GABA (VGAT), and acetylcholine (VACht) transporters in basal forebrain axon terminals innervating the lateral hypothalamus. Journal of Comparative Neurology *496*, 453-467.
Hikosaka, O. (2010). The habenula: from stress evasion to value-based decision-making. Nature reviews Neuroscience *11*, 503-513.
Hobson, J.A. (2005). Sleep is of the brain, by the brain and for the brain. Nature *437*, 1254-1256.
Huang, Z.J., and Zeng, H. (2013). Genetic approaches to neural circuits in the mouse. Annu Rev Neurosci *36*, 183-215.
Jones, B.E. (2011). Chapter 9 - Neurobiology of waking and sleeping. In Handbook of Clinical Neurology, P. Montagna, and S. Chokroverty, eds. (Elsevier), pp. 131-149.
Jones, B.E., and Cuello, A.C. (1989). Afferents to the basal forebrain cholinergic cell area from pontomesencephalic—catecholamine, serotonin, and acetylcholine—neurons. Neuroscience *31*, 37-61.
Kasckow, J., and Nemeroff, C.B. (1991). The neurobiology of neurotensin: focus on neurotensin-dopamine interactions. Regulatory peptides *36*, 153-164.
Kim, T., Thankachan, S., McKenna, J.T., McNally, J.M., Yang, C., Choi, J.H., Chen, L., Kocsis, B., Deisseroth, K., Strecker, R.E.*, et al.* (2015). Cortically projecting basal forebrain parvalbumin neurons regulate cortical gamma band oscillations. Proceedings of the National Academy of Sciences *112*, 3535.
Kimura, M., Muller-Preuss, P., Lu, A., Wiesner, E., Flachskamm, C., Wurst, W., Holsboer, F., and Deussing, J.M. (2010). Conditional corticotropin-releasing hormone overexpression in the mouse forebrain enhances rapid eye movement sleep. Molecular psychiatry *15*, 154-165.
Konopka, R.J., and Benzer, S. (1971). Clock mutants of Drosophila melanogaster. Proceedings of the National Academy of Sciences of the United States of America *68*, 2112-2116.
Krueger, J.M., Obal, F., Jr., and Fang, J. (1999). Humoral regulation of physiological sleep: cytokines and GHRH. Journal of sleep research *8 Suppl 1*, 53-59.
Krueger, J.M., Walter, J., Dinarello, C.A., Wolff, S.M., and Chedid, L. (1984). Sleep-promoting effects of endogenous pyrogen (interleukin-1). The American journal of physiology *246*, R994-

999.
Laposky, A., Easton, A., Dugovic, C., Walisser, J., Bradfield, C., and Turek, F. (2005). Deletion of the mammalian circadian clock gene BMAL1/Mop3 alters baseline sleep architecture and the response to sleep deprivation. Sleep *28*, 395-409.
Lee, M.G., Hassani, O.K., Alonso, A., and Jones, B.E. (2005). Cholinergic basal forebrain neurons burst with theta during waking and paradoxical sleep. The Journal of neuroscience : the official journal of the Society for Neuroscience *25*, 4365-4369.
Leinninger, G.M., Opland, D.M., Jo, Y.H., Faouzi, M., Christensen, L., Cappellucci, L.A., Rhodes, C.J., Gnegy, M.E., Becker, J.B., Pothos, E.N.*, et al.* (2011). Leptin action via neurotensin neurons controls orexin, the mesolimbic dopamine system and energy balance. Cell metabolism *14*, 313-323.
Lin, S.-C., Brown, R.E., Hussain Shuler, M.G., Petersen, C.C.H., and Kepecs, A. (2015). Optogenetic Dissection of the Basal Forebrain Neuromodulatory Control of Cortical Activation, Plasticity, and Cognition. The Journal of Neuroscience *35*, 13896.
Lin, S.-C., and Nicolelis, M.A.L. (2008). Neuronal Ensemble Bursting in the Basal Forebrain Encodes Salience Irrespective of Valence. Neuron *59*, 138-149.
Liu, Z.W., and Gao, X.B. (2007). Adenosine inhibits activity of hypocretin/orexin neurons by the A1 receptor in the lateral hypothalamus: a possible sleep-promoting effect. Journal of neurophysiology *97*, 837-848.
Lu, J., Zhang, Y.H., Chou, T.C., Gaus, S.E., Elmquist, J.K., Shiromani, P., and Saper, C.B. (2001). Contrasting Effects of Ibotenate Lesions of the Paraventricular Nucleus and Subparaventricular Zone on Sleep–Wake Cycle and Temperature Regulation. The Journal of neuroscience : the official journal of the Society for Neuroscience *21*, 4864-4874.
Manns, I.D., Mainville, L., and Jones, B.E. (2001). Evidence for glutamate, in addition to acetylcholine and GABA, neurotransmitter synthesis in basal forebrain neurons projecting to the entorhinal cortex. Neuroscience *107*, 249-263.
Mansbach, R.S., and Lorenz, D.N. (1983). Cholecystokinin (CCK-8) elicits prandial sleep in rats. Physiology & behavior *30*, 179-183.
McDonald, M.J., and Rosbash, M. (2001). Microarray analysis and organization of circadian gene expression in Drosophila. Cell *107*, 567-578.
McGaughy, J., Kaiser, T., and Sarter, M. (1996). Behavioral vigilance following infusions of 192 IgG-saporin into the basal forebrain: selectivity of the behavioral impairment and relation to cortical AChE-positive fiber density. Behavioral neuroscience *110*, 247-265.
McGinty, D.J., and Sterman, M.B. (1968). Sleep suppression after basal forebrain lesions in the cat. Science (New York, NY) *160*, 1253-1255.
Menegas, W., Bergan, J.F., Ogawa, S.K., Isogai, Y., Umadevi Venkataraju, K., Osten, P., Uchida, N., and Watabe-Uchida, M. (2015). Dopamine neurons projecting to the posterior striatum form an anatomically distinct subclass. eLife *4*, e10032.
Mesulam, M.M., and Mufson, E.J. (1984). Neural inputs into the nucleus basalis of the substantia innominata (Ch4) in the rhesus monkey. Brain : a journal of neurology *107 (Pt 1)*, 253-274.
Miyamichi, K., Amat, F., Moussavi, F., Wang, C., Wickersham, I., Wall, N.R., Taniguchi, H., Tasic, B., Huang, Z.J., He, Z.*, et al.* (2011). Cortical representations of olfactory input by trans-synaptic tracing. Nature *472*, 191-196.

Miyamichi, K., Shlomai-Fuchs, Y., Shu, M., Weissbourd, B.C., Luo, L., and Mizrahi, A. (2013). Dissecting local circuits: parvalbumin interneurons underlie broad feedback control of olfactory bulb output. Neuron *80*, 1232-1245.
Moruzzi, G., and Magoun, H.W. (1949). Brain stem reticular formation and activation of the EEG. Electroencephalography and clinical neurophysiology *1*, 455-473.
Nauta, W.J. (1946). Hypothalamic regulation of sleep in rats; an experimental study. Journal of neurophysiology *9*, 285-316.
Naylor, E., Bergmann, B.M., Krauski, K., Zee, P.C., Takahashi, J.S., Vitaterna, M.H., and Turek, F.W. (2000). The circadian clock mutation alters sleep homeostasis in the mouse. The Journal of neuroscience : the official journal of the Society for Neuroscience *20*, 8138-8143.
Nguyen, D.P., and Lin, S.C. (2014). A frontal cortex event-related potential driven by the basal forebrain. eLife *3*, e02148.
Nitz, D., and Siegel, J.M. (1996). GABA release in posterior hypothalamus across sleep-wake cycle. The American journal of physiology *271*, R1707-1712.
O'Neill, J.S., Maywood, E.S., Chesham, J.E., Takahashi, J.S., and Hastings, M.H. (2008). cAMP-dependent signaling as a core component of the mammalian circadian pacemaker. Science (New York, NY) *320*, 949-953.
Ogawa, Sachie K., Cohen, Jeremiah Y., Hwang, D., Uchida, N., and Watabe-Uchida, M. (2014). Organization of Monosynaptic Inputs to the Serotonin and Dopamine Neuromodulatory Systems. Cell Reports *8*, 1105-1118.
Oh, S.W., Harris, J.A., Ng, L., Winslow, B., Cain, N., Mihalas, S., Wang, Q., Lau, C., Kuan, L., Henry, A.M*., et al.* (2014). A mesoscale connectome of the mouse brain. Nature *508*, 207-214.
Oishi, Y., Huang, Z.L., Fredholm, B.B., Urade, Y., and Hayaishi, O. (2008). Adenosine in the tuberomammillary nucleus inhibits the histaminergic system via A1 receptors and promotes non-rapid eye movement sleep. Proceedings of the National Academy of Sciences of the United States of America *105*, 19992-19997.
Osten, P., and Margrie, T.W. (2013). Mapping brain circuitry with a light microscope. Nature methods *10*, 515-523.
Pan, W.J., Osmanovic, S.S., and Shefner, S.A. (1995). Characterization of the adenosine A1 receptor-activated potassium current in rat locus ceruleus neurons. The Journal of pharmacology and experimental therapeutics *273*, 537-544.
Paré, D., and Smith, Y. (1994). GABAergic projection from the intercalated cell masses of the amygdala to the basal forebrain in cats. Journal of Comparative Neurology *344*, 33-49.
Parent, A., Paré, D., Smith, Y., and Steriade, M. (1988). Basal forebrain cholinergic and noncholinergic projections to the thalamus and brainstem in cats and monkeys. Journal of Comparative Neurology *277*, 281-301.
Patke, A., Murphy, P.J., Onat, O.E., Krieger, A.C., Ozcelik, T., Campbell, S.S., and Young, M.W. (2017). Mutation of the Human Circadian Clock Gene CRY1 in Familial Delayed Sleep Phase Disorder. Cell *169*, 203-215.e213.
Peterfi, Z., McGinty, D., Sarai, E., and Szymusiak, R. (2010). Growth hormone-releasing hormone activates sleep regulatory neurons of the rat preoptic hypothalamus. American journal of physiology Regulatory, integrative and comparative physiology *298*, R147-156.
Peyron, C., Tighe, D.K., van den Pol, A.N., de Lecea, L., Heller, H.C., Sutcliffe, J.G., and Kilduff, T.S. (1998). Neurons containing hypocretin (orexin) project to multiple neuronal systems. The

Journal of neuroscience : the official journal of the Society for Neuroscience *18*, 9996-10015.
Phillips, A.J., Fulcher, B.D., Robinson, P.A., and Klerman, E.B. (2013). Mammalian rest/activity patterns explained by physiologically based modeling. PLoS Comput Biol *9*, e1003213.
Pollak Dorocic, I., Fürth, D., Xuan, Y., Johansson, Y., Pozzi, L., Silberberg, G., Carlén, M., and Meletis, K. (2014). A Whole-Brain Atlas of Inputs to Serotonergic Neurons of the Dorsal and Median Raphe Nuclei. Neuron *83*, 663-678.
Porkka-Heiskanen, T., Strecker, R.E., Thakkar, M., Bjorkum, A.A., Greene, R.W., and McCarley, R.W. (1997). Adenosine: a mediator of the sleep-inducing effects of prolonged wakefulness. Science (New York, NY) *276*, 1265-1268.
Ralph, M.R., Foster, R.G., Davis, F.C., and Menaker, M. (1990). Transplanted suprachiasmatic nucleus determines circadian period. Science (New York, NY) *247*, 975-978.
Reppert, S.M., and Weaver, D.R. (2001). Molecular analysis of mammalian circadian rhythms. Annual review of physiology *63*, 647-676.
Robledo, P., Kaneko, W.M., and Ehlers, C.L. (1995). Effects of neurotensin on EEG and event-related potentials in the rat. Psychopharmacology *118*, 410-418.
Rye, D.B., Wainer, B.H., Mesulam, M.M., Mufson, E.J., and Saper, C.B. (1984). Cortical projections arising from the basal forebrain: A study of cholinergic and noncholinergic components employing combined retrograde tracing and immunohistochemical localization of choline acetyltransferase. Neuroscience *13*, 627-643.
Sallanon, M., Denoyer, M., Kitahama, K., Aubert, C., Gay, N., and Jouvet, M. (1989). Long-lasting insomnia induced by preoptic neuron lesions and its transient reversal by muscimol injection into the posterior hypothalamus in the cat. Neuroscience *32*, 669-683.
Saper, C.B. (1985). Organization of cerebral cortical afferent systems in the rat. II. Hypothalamocortical projections. The Journal of comparative neurology *237*, 21-46.
Saper, C.B., Chou, T.C., and Scammell, T.E. (2001). The sleep switch: hypothalamic control of sleep and wakefulness. Trends in neurosciences *24*, 726-731.
Saper, C.B., Fuller, P.M., Pedersen, N.P., Lu, J., and Scammell, T.E. (2010). Sleep State Switching. Neuron *68*, 1023-1042.
Sarter, M., Givens, B., and Bruno, J.P. (2001). The cognitive neuroscience of sustained attention: where top-down meets bottom-up. Brain Research Reviews *35*, 146-160.
Savage, V.M., and West, G.B. (2007). A quantitative, theoretical framework for understanding mammalian sleep. Proceedings of the National Academy of Sciences *104*, 1051-1056.
Schliebs, R., and Arendt, T. (2011). The cholinergic system in aging and neuronal degeneration. Behavioural brain research *221*, 555-563.
Semba, K. (2000). Multiple output pathways of the basal forebrain: organization, chemical heterogeneity, and roles in vigilance. Behavioural brain research *115*, 117-141.
Semba, K., Reiner, P.B., McGeer, E.G., and Fibiger, H.C. (1988). Brainstem afferents to the magnocellular basal forebrain studied by axonal transport, immunohistochemistry, and electrophysiology in the rat. Journal of Comparative Neurology *267*, 433-453.
Sherin, J.E., Elmquist, J.K., Torrealba, F., and Saper, C.B. (1998). Innervation of histaminergic tuberomammillary neurons by GABAergic and galaninergic neurons in the ventrolateral preoptic nucleus of the rat. The Journal of neuroscience : the official journal of the Society for Neuroscience *18*, 4705-4721.
Sherin, J.E., Shiromani, P.J., McCarley, R.W., and Saper, C.B. (1996). Activation of ventrolateral

preoptic neurons during sleep. Science (New York, NY) *271*, 216-219.
Strecker, R.E., Morairty, S., Thakkar, M.M., Porkka-Heiskanen, T., Basheer, R., Dauphin, L.J., Rainnie, D.G., Portas, C.M., Greene, R.W., and McCarley, R.W. (2000). Adenosinergic modulation of basal forebrain and preoptic/anterior hypothalamic neuronal activity in the control of behavioral state. Behavioural brain research *115*, 183-204.
Szymusiak, R., and McGinty, D. (1986). Sleep-related neuronal discharge in the basal forebrain of cats. Brain research *370*, 82-92.
Szymusiak, R., and McGinty, D. (2008). Hypothalamic regulation of sleep and arousal. Annals of the New York Academy of Sciences *1129*, 275-286.
Taniguchi, H., He, M., Wu, P., Kim, S., Paik, R., Sugino, K., Kvitsani, D., Fu, Y., Lu, J., Lin, Y.*, et al.* (2011). A Resource of Cre Driver Lines for Genetic Targeting of GABAergic Neurons in Cerebral Cortex. Neuron *71*, 995-1013.
Uhl, G.R., and Snyder, S.H. (1976). Regional and subcellular distributions of brain neurotensin. Life sciences *19*, 1827-1832.
Vitaterna, M.H., King, D.P., Chang, A.-M., Kornhauser, J.M., Lowrey, P.L., McDonald, J.D., Dove, W.F., Pinto, L.H., Turek, F.W., and Takahashi, J.S. (1994). Mutagenesis and Mapping of a Mouse Gene, Clock, Essential for Circadian Behavior. Science (New York, NY) *264*, 719-725.
Wall, N.R., De La Parra, M., Callaway, E.M., and Kreitzer, A.C. (2013). Differential innervation of direct- and indirect-pathway striatal projection neurons. Neuron *79*, 347-360.
Watabe-Uchida, M., Zhu, L., Ogawa, Sachie K., Vamanrao, A., and Uchida, N. (2012). Whole-Brain Mapping of Direct Inputs to Midbrain Dopamine Neurons. Neuron *74*, 858-873.
Weissbourd, B., Ren, J., DeLoach, Katherine E., Guenthner, Casey J., Miyamichi, K., and Luo, L. (2014). Presynaptic Partners of Dorsal Raphe Serotonergic and GABAergic Neurons. Neuron *83*, 645-662.
Wenk, G.L. (1997). The Nucleus Basalis Magnocellularis Cholinergic System: One Hundred Years of Progress. Neurobiology of Learning and Memory *67*, 85-95.
Whitehouse, P.J., Price, D.L., Struble, R.G., Clark, A.W., Coyle, J.T., and Delon, M.R. (1982). Alzheimer's disease and senile dementia: loss of neurons in the basal forebrain. Science (New York, NY) *215*, 1237.
Wickersham, I.R., Lyon, D.C., Barnard, R.J.O., Mori, T., Finke, S., Conzelmann, K.-K., Young, J.A.T., and Callaway, E.M. (2007). Monosynaptic Restriction of Transsynaptic Tracing from Single, Genetically Targeted Neurons. Neuron *53*, 639-647.
Xu, M., Chung, S., Zhang, S., Zhong, P., Ma, C., Chang, W.C., Weissbourd, B., Sakai, N., Luo, L., Nishino, S.*, et al.* (2015). Basal forebrain circuit for sleep-wake control. Nature neuroscience *18*, 1641-1647.
Yang, C., McKenna, J.T., Zant, J.C., Winston, S., Basheer, R., and Brown, R.E. (2014). Cholinergic neurons excite cortically projecting basal forebrain GABAergic neurons. The Journal of neuroscience : the official journal of the Society for Neuroscience *34*, 2832-2844.
Young, M.W., and Kay, S.A. (2001). Time zones: a comparative genetics of circadian clocks. Nature reviews Genetics *2*, 702-715.
Za´borsky, L.s., and Cullinan, W.E. (1992). Projections from the nucleus accumbens to cholinergic neurons of the ventral pallidum: a correlated light and electron microscopic double-immunolabeling study in rat. Brain research *570*, 92-101.
Zaborszky, L., and Duque, A. (2000). Local synaptic connections of basal forebrain neurons.

Behavioural brain research *115*, 143-158.
Zaborszky, L., Gaykema, R.P., Swanson, D.J., and Cullinan, W.E. (1997). Cortical input to the basal forebrain. Neuroscience *79*, 1051-1078.
Zhang, J., Obal, F., Jr., Zheng, T., Fang, J., Taishi, P., and Krueger, J.M. (1999). Intrapreoptic microinjection of GHRH or its antagonist alters sleep in rats. The Journal of neuroscience : the official journal of the Society for Neuroscience *19*, 2187-2194.